Thesis for the degree of Doctor of Philosophy

Modelling optical properties of morphologically complex aerosols

Franz Kanngießer

Department of Space, Earth and Environment
CHALMERS UNIVERSITY OF TECHNOLOGY
Göteborg, Sweden 2021

Modelling optical properties of morphologically complex aerosols
Franz Kanngiesser
ISBN 978-91-7905-592-9

Doktorsavhandlingar vid Chalmers tekniska högskola
Ny serie nr 5059
ISSN 0346-718X

Department of Space, Earth and Environment
Chalmers University of Technology
SE–412 96 Göteborg, Sweden
Telephone + 46 (0) 31 – 772 1000

Example of morphologically complex aerosol particles used in this thesis

Typeset by the author using LaTeX.

Printed by Chalmers Digitaltryck
Göteborg, Sweden 2021

Modelling optical properties of morphologically complex aerosols
Franz Kanngiesser
Department of Space, Earth and Environment
Chalmers University of Technology

Abstract

The interpretation of remote sensing data of atmospheric aerosol particles requires a thorough understanding of the links between microphysical and optical properties. Morphologically complex aerosol models describe the particles' morphology in detail. Based on the calculations with realistic particle models, simplified models can be devised, which incorporate essential microphysical properties for reproducing the optical properties. In this thesis, such models are developed and tested for soot aerosols, for mineral dust, and for dried and partially dissolved sea salt aerosol.

A tunable model for coated soot aggregates is presented, and corresponding uncertainty estimates are performed. One of the main sources of uncertainty for thickly coated soot is the chemical composition of the coating, as represented by its refractive index. These uncertainties are so substantial, they are investigated as a potential source of information. The calculated lidar-measurable (spectral) quantities are distinct for two coating materials.

The non-sphericity of a particle is identified as an essential morphological property affecting the linear depolarisation ratio. For coated soot another important property is the amount of carbon interacting with the incident wave, as it affects the absorption cross section. Combining these two insights resulted in the core grey shell dimer (CGS2) model, which is introduced in this thesis.

For dry sea salt aerosol different random geometries are investigated, to simultaneously calculate linear depolarisation and extinction-to-backscatter ratio of dried sea salt aerosol particles. The results indicate that convex polyhedra are best suited to represent dried sea salt aerosol particles. Thus, the coated convex polyhedra model is proposed as the basis for modelling dissolving sea salt in a further study. For dissolving sea salt three simplified, equally well-performing models are presented, which identify the change in particle sphericity as a key morphological feature.

A spheroidal model with a single refractive index and a single aspect ratio is fitted to laboratory measurements of 131 different dust samples. The scattering of the measurements about the model can mainly be explained by changes in morphology and dielectric properties, and to a lesser degree by the width of the particle size distribution.

These results are expected to significantly advance our capacity to exploit and interpret polarimetric remote sensing observations of morphologically complex and chemically heterogeneous aerosol. This will be important for constraining Earth-system climate and air-quality forecasting models, and for evaluating and improving parameterisations of aerosol processes in these environmental modelling systems.

Keywords: aerosol, depolarisation, scattering, remote sensing, black carbon, sea salt, mineral dust.

List of Publications

This thesis is based on the following appended papers:

Paper A. Franz Kanngießer and Michael Kahnert. *Calculation of optical properties of light-absorbing carbon with weakly absorbing coating: A model with tunable transition from film-coating to spherical-shell coating.* J. Quant. Spectrosc. Radiat. Transfer, 216, 17–36, 2018.

Paper B. Franz Kanngießer and Michael Kahnert. *Coating material-dependent differences in modelled lidar-measurable quantities for heavily coated soot particles.* Opt. Express, 21, 36368–36387, 2019.

Paper C. Michael Kahnert and Franz Kanngießer. *Aerosol optics model for black carbon applicable to remote sensing, chemical data assimilation, and climate modelling* Opt. Express, 29, 10639–10658, 2021.

Paper D Michael Kahnert, Franz Kanngießer, Emma Järvinen and Martin Schnaiter. *Aerosol-optics model for the backscatter depolarisation ratio of mineral dust particles* J. Quant. Spectrosc. Radiat. Transfer, 254, 107177, 2020.

Paper E Franz Kanngießer and Michael Kahnert. *Modeling optical properties of non-cubical sea salt particles* J. Geophys. Res. Atmos., 126, e2020JD033674, 2021

Paper F Franz Kanngießer and Michael Kahnert. *Optical properties of water-coated sea salt model particles* Opt. Express, 29, 34926–34950, 2021.

Other publications co-authored by Franz Kanngießer:

Michael Kahnert and Franz Kanngießer. *Modelling optical properties of atmospheric black carbon aerosols* J. Quant. Spectrosc. Radiat. Transfer, 244, 106849, 2020 (Invited Review).

Contents

Acknowledgments

While only my name is printed on the cover and the spine of this thesis, there are several people, who contributed directly and indirectly to my journey during the last four and a half years. This journey resulted in this thesis. First and foremost, I am grateful to have been given this opportunity.

I want to thank my main supervisor Michael for the fruitful discussions, his feedback, support, and time. In addition, I would also like to thank Patrick and Donal, my assistant supervisor and examiner respectively, for their input, support, and feedback.

There were and there still are several other people at the department, with whom I had interesting discussions. Most of these discussions are not directly reflected in the actual content of this thesis, but they allowed me to test ideas, get a better understanding of different (side-)topics, get new inspirations, find the eventually successful way to tackle coding/computation issues, navigating course choices or learn something new. For these discussions, I would like to thank (in no particular order) Robert, Simon, Robin, Anqi, David, Vasileios, Albert, Anis, Boy, Grzegorz, Anders, Joakim, Jana, Emil, David, Ole Martin, Francesco, and everyone else I might have forgotten on this list. Emil, Olof, and Vasileios also helped to improve this thesis by proofreading parts of it.

I would also like to thank all the regular and not so regular *fika* attendees on floor 4ö and in various Zoom rooms for all the different conversations and the possibilities to practice Swedish.

Finally, I would like my friends and family for encouraging me to embark on and supporting me during this journey.

Franz Kanngießer
Göteborg, November 2021

Part I

Introductory chapters

Chapter 1

Introduction

Small particles suspended in the air, atmospheric aerosol particles, have wide ranging effects. Among these effects are adverse impacts on air quality and human health and impacts on the Earth's climate system. They even affected culture - for example as descriptions of London's smog in the literary works by Dickens and Conan Doyle (Fowler et al. 2020) or optical effects of volcanic ash can be traced to paintings by, among others, Turner and Friedrich (Zerefos et al. 2007).

Aerosol particles have predominantly a cooling effect on the Earth's climate. Cooling by anthropogenic aerosol, which can be traced back to about 1750, partially counteracts the warming effect of greenhouse gases. One notable exception is black carbon (or soot), which has a warming effect, as quantified by its positive effective radiative forcing (Forster et al. 2021; Naik et al. 2021).

Air pollution is one of the largest environmental risk factors for human health (Murray et al. 2020; World Health Organization 2016). Air pollution as an umbrella term includes topics beyond the scope of this work, such as gaseous material or indoor air pollution (Murray et al. 2020). However, to get a first idea of the scale of air pollution, it should be noted that half of the world's pollution is exposed to increasing air pollution (Shaddick et al. 2020). According to the Global Burden of Diseases database of 2019 (Murray et al. 2020) the risk factor on human health associated with ambient particulate matter, pertaining to what is here referred to as atmospheric aerosol particles, increased since 1990. For comparison the risk factor associated with household, i.e. indoor, air pollution fell in the same time span.

Both the impacts on human health and climate highlight the need of reliable observations to improve the understanding of aerosol processes and trends. Satellite observations are capable of providing consistent long-term observations with a large geographical, depending on the satellite, even nearly global, coverage. Such observations and subsequent detailed studies require robust optical models, which capture the essential morphological and compositional properties, i.e., those microphysical characteristics that most strongly impact the optical properties. A particularly strong focus in the thesis is placed on the linear depolarisation ratio. It quantifies changes in the polarisation state of fully polarised laser light due to scattering by aerosol particles. A long term goal, to which this thesis aims to contribute, is the assimilation of lidar measurements into chemical transport models. These methods

aim at constraining and improving air-quality forecasts. A robust aerosol optics model is one essential component in an aerosol assimilation system. Another, equally important prerequisite for data assimilation is a robust estimate of the optics model's uncertainties.

Chapter 2 gives a brief introduction to the Earth's atmosphere and to atmospheric aerosol. A short overview over remote sensing of aerosol is presented in Chapter 3. The physical conceptualisation of remote sensing relies on radiative transfer, and the interpretation of remote sensing data requires an understanding of the particle's single scattering properties, both topics are introduced in Chapter 4. Chapter 5 discusses particle models used earlier to calculate optical properties of aerosol particles with a focus on soot, mineral dust and sea salt aerosol. The appended articles (Papers A - F) are summarised in chapter 6. The final chapter, Chapter 7, gives a short conclusion as well as an outlook.

Chapter 2

The Earth's atmosphere

The Earth's atmosphere consists of 78% of nitrogen (N_2), to 21% of oxygen (O_2), to 1% of Argon (Ar), and of less than 1% of various trace gases. These trace gases can have a considerable impact on the Earth's radiative balance and consequently the climate. Examples are carbon dioxide (CO_2) or methane (CH_4). Methane and other trace gases affect air quality (Seinfeld and Pandis 2016). When neglecting water vapour, the (dry) atmosphere can be considered largely well-mixed, up to an altitude of around 100 km. That means that the volume mixing ratio of the gaseous components is constant with height.

With increasing height the pressure $p(Z)$ decreases exponentially and can be calculated as (Holton 2004):

$$p(Z) = p(0) \exp\left(\frac{-Z g_0}{R\bar{T}}\right) \tag{2.1}$$

The pressure at surface level is commonly assumed to take the value of the global mean with $p(0) = 1013.25\,\mathrm{hPa}$. Here, Z is the geopotential height, which can be seen as a gravity-adjusted height[1]. The global average of the gravitational accelaration at sea level is denoted as g_0, with $g_0 = 9.80665\,\mathrm{m\,s^{-2}}$. $\bar{T}$ is the layer mean temperature. The vertical change of the temperature can be used for determining the atmosphere's vertical structure (see Section 2.1). R is the specific gas constant for dry air, with $R = 287\,\mathrm{J\,kg^{-1}\,K^{-1}}$.

2.1 Atmospheric structure

Based on the changes of the temperature's vertical gradient, the atmosphere can be divided into several sub-layers. These changes in temperature gradient are called (temperature) inversion. Inversions, especially strong inversions cap upward motion of air. Consequently, there is only limited exchange of mass between the different layers of the atmosphere (Stull 1988; Wells 2011). The lowest level of the atmosphere, the troposphere, is characterised by a negative temperature gradient, i.e. an decrease

[1]The geometrical height z and the geopotential height are numerically almost identical. The geopotential Φ can be calculated from $\mathrm{d}\Phi = g\mathrm{d}z$ and the geopotential height is $Z = \Phi(z)/g_0$.

of temperature with increasing height. The cause for this is the increasing distance from the Earth's surface, which is warmed by solar radiation and re-emits thermal radiation (Seinfeld and Pandis 2016). Commonly the troposphere is considered to have a height of about 10 kilometres (Holton 2004), but varies between about 9 km at the poles and about 17 km at the equator (World Meteorological Organization 1992). In the stratosphere, the layer above the troposphere, the temperature increases with height. This is caused by absorption and by photodissociation of ozone, which occurs mainly in the ozone layer with the maximum of the ozone concentration at a height of 20-30 km. Ozone is highly reactive, preventing it from remaining long enough in the atmosphere to become well-mixed (Seinfeld and Pandis 2016; Wells 2011). The stratosphere is followed by the mesosphere and the thermosphere. The upper boundary of each layer, referred to as *-pause* , i.e. the tropopause between troposphere and stratosphere or the stratopause between the stratosphere and the mesosphere, is defined by the point, at which the temperature gradient changes abruptly[2]. Figure 2.1 shows the vertical profile of the temperature in K (red) and the pressure in hPa (blue) as defined in the US Standard Atmosphere of 1976. Horizontal lines indicate the position of the tropopause, stratopause, and mesopause. The US Standard Atmosphere is an idealised, seasonally averaged representation of the atmosphere. It is based on observations and gives the conditions for a geographical latitude of 45°N.

Water vapour is another component of the atmosphere, which is not well-mixed, but highly variable. Its mass fraction ranges from 0 to 4.3%. The maximum amount of water vapour in the atmosphere depends on the ambient air temperature. This temperature dependence prevents water vapour from being a well-mixed component of the atmosphere. As can be seen in Fig. 2.1, the tropospheric temperature decreases with height, so does consequently the water vapour content. In case of the US Standard Atmosphere (1976) $\sim 90\%$ of the water vapour mass are concentrated within the atmosphere's lowest five kilometres (U.S. Commitee on Extension of the Standard Atmosphere 1976).

In addition to dividing the atmosphere into different layers according to the temperature gradient, the atmosphere can also be divided with respect to the influence of the Earth's surface on the atmosphere. This results in two layers, the (planetary) boundary layer (PBL) and the free atmosphere. Within the boundary layer the atmosphere is directly influenced by the presence of the Earth's surface. Further, the atmosphere responds to surface forcings with time-scales of up to an hour, such as frictional drag, evaporation, transpiration, heat fluxes, pollutant emission, and flow modifications induced by terrain changes (Holton 2004; Stull 1988).

The transition from the PBL to the free atmosphere is often characterised by a temperature inversion. As mentioned earlier, temperature inversions suppress upward movement of air masses, including the moisture and particles contained in them (Stull 1988), which leads to the PBL having the highest aerosol particle loads (McCormick and Leavor 2013). As a consequence of the suppressed upward motion,

[2]The World Meteorological Organisation defines the tropopause as the lowest level, at which the temperature gradient's absolute value is below 2 Kelvin per kilometre (World Meteorological Organization 1992).

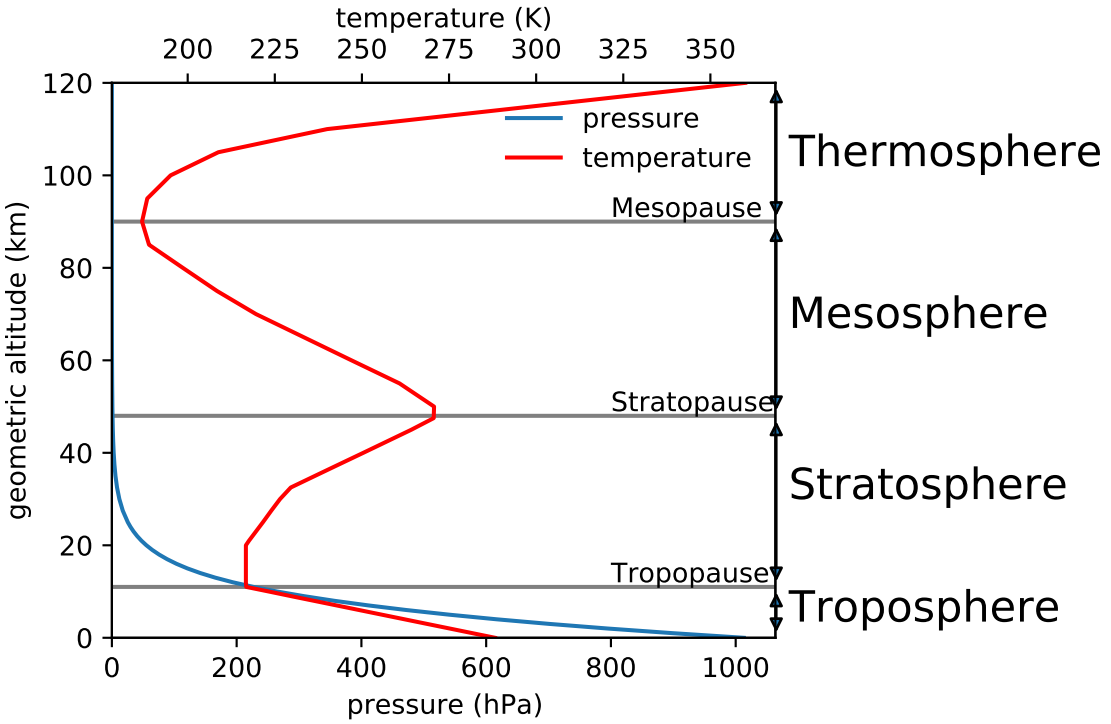

Figure 2.1: Temperature (red) and pressure (blue) with height as defined in the US Standard Atmosphere (1972). The vertical lines indicate the transitions between atmospheric layers. Image created by the author.

strato-cumulus clouds frequently form at the top of the PBL. The PBL can also be defined according to the impacts on the strato-cumulus cloud layer (Wood 2012). The height of the PBL may range from 30 m up to 3 km, but its average in the mid-latitudes is about 1 km (Holton 2004; Stull 1988). As the top of the PBL is always within the troposphere, the PBL might also be considered a subdivision of the troposphere. Conditions within the boundary affect the formation of particles and growth or other changes of particles emitted into the atmosphere (Boucher 2015).

Another subdivision of the troposphere can be observed in the tropics. About 80% of all soundings above the tropical[3] oceans show a strong inversion within the lower troposphere. In the trade wind region this inversion is called trade wind inversion (Krishnamurti et al. 2013). The trade wind inversion does not necessarily, but may coincide with the inversion on top of the planetary boundary layer (Carrillo et al. 2016). The trade wind inversion is hypothesised to dry aerosol particles such as marine aerosol particles (Haarig et al. 2017).

[3]While the area between the Tropic of Cancer or Northern Tropic at 23.5° N and the Tropic of Capricorn or Southern Tropic at 23.5° S is commonly (see for example the Oxford English Dictionary or the Merriam-Webster Dictionary) considered as the tropics, this thesis, however, follows a common definition within meteorology to consider the area between 30 °N and 30°S as tropics. Thus, with this definition the tropics cover half of the Earth's surface.

2.2 Atmospheric Aerosol

The term aerosol refers to particles, both liquid and solid, suspended in a fluid and the fluid containing the particles. Hydrometeors, such as cloud droplets, cloud ice, and precipitation in all its various forms are, by convention in atmospheric science, not considered to be aerosol particles, even if they meet the definition.

Owning to the very broad definition of aerosol there are multiple ways to classify aerosol particles (Boucher 2015). Aerosols can be classified for example according to their formation process as primary, i.e. emitted as particle, or secondary, i.e., formed as particle within the atmosphere from precursor gases. Alternatively, they can be classified by their environment, such as urban, rural, desert, etc. aerosol particles.

Aerosol particles can typically be found in the troposphere and the stratosphere. Usually aerosol particles and their precursors are directly emitted into the troposphere. Stratospheric aerosol is, in general, linked to volcanic eruptions, but deep convection in the tropics and convection caused by wildfires can also inject aerosol particles into the stratosphere (Boucher 2015; Yu et al. 2019). The life time of tropospheric aerosol particles is between a few days to up to two weeks. However, in the stratosphere aerosol particles remain for six month up to two years. Mechanisms causing the removal of aerosol particles are wet deposition (i.e., being washed out), dry deposition (i.e., carried to the ground by turbulent fluxes), and sedimentation (i.e., being deposited by gravity) (Boucher 2015).

2.2.1 Aerosol sources

In addition to the distinction between primary and secondary aerosol, aerosol particles can also be classified according to their source. The most common aerosol types are mineral dust, marine, biogenic, biomass burning, anthropogenic burning, and volcanic aerosol. Marine or sea spray aerosol originate from sea water ejected from the ocean by bursting air bubbles in the ocean and by wind tearing off wave crests. It is dominated by sea salt, but may contain biogenic material, dimethyl sulfide, and other impurities, originating from plankton. Annually between 1000 - 6000 Tg (1 Tg $= 10^{12}$ g = 1,000,000 tons) of sea spray aerosol are emitted. Seas and oceans are also an important source of precursor material. Typically marine aerosol particles range between 100 nm and tens of microns in size.

Wind friction also causes desert dust or mineral dust emissions from arid, semi-arid, and desertic regions to be lifted off the ground. About 1000 - 3000 Tg are emitted into the atmosphere per year. Mineral dust aerosol has a similar size range as marine aerosol particles.

Volcanic eruptions eject volcanic ash, pulverised rock fragments, and minerals into the atmosphere. The resulting aerosol particles tend to cover a size range between a few micrometers to millimetres. Volcanoes also emit sulphur-containing gases, which act as precursor or can condense onto other aerosol particles. Due to the longer residence time in the stratosphere, as discussed earlier, volcanic eruptions can have a considerable effect on the Earth's climate.

Pollen, spores, bacteria, viruses, and debris of plants and insects constitute biogenic aerosol. Per year approximately 1000 Tg biogenic aerosol particles are emitted, including estimated 40 - 1800 Gg bacteria (1 Gg = 10^9 g = 1,000 tons) and 30 Tg spores. Due to the variety of biogenic aerosol particles, there are different typical size ranges. Viruses and small bacteria are usually smaller than 1 μm. Larger bacteria, pollen, and spores have a size between 1 and 100 μm. Even larger are plant and insect debris, which as a consequence tend to have a shorter residence time in the atmosphere. Ecosystems, including marine ecosystems, may also be an important source of secondary biogenic aerosol.

Aerosols from biomass burning and fossil fuel combustion contain both black and organic carbon. Organic carbon and black carbon differ in their chemical composition, organic carbon contains a relatively high number fraction of oxygen and hydrogen atoms, while black carbon possesses a higher number fraction of carbon atoms. Carbonaceous aerosol particles are usually smaller than one micrometre. The estimated annual emission flux of biomass burning aerosol is 70 - 125 Tg, and 26-40 Tg for fossil fuel combustion aerosol. Burning fossil fuels and biomass also releases of precursor gases.

2.2.2 Aerosol effects

Since aerosol particles are diverse in their origin, their chemical composition, and their microphysical properties, they have wide-ranging impacts.

Aerosol particles scatter and absorb solar radiation directly, as is well documented for sea salt aerosol (Buseck and Pósfai 1999; King et al. 2012; Murphy et al. 1998), mineral dust, especially in form of dust storms (Goudie 2009; Kumar et al. 2014), or black carbon (Bond et al. 2013; Bond and Bergstrom 2006). This absorption and scattering of solar radiation by aerosol particles, in turn, affects the atmosphere and more broadly the climate system. Absorption by aerosol particles changes the atmospheric temperature profile. This affects relative humidity and atmospheric stability, which then impacts cloud formation processes (Boucher 2015). Cloud formation processes are additionally impacted by aerosol particles, such as black carbon, mineral dust, marine aerosol and biogenic aerosol, serving as cloud condensation nucleii and ice nucleii (e.g. Boucher 2015; Hoose et al. 2010; Murray et al. 2012; Steiner et al. 2015). An increase in the number of cloud condensation nucleii leads to an increase in cloud droplet concentration. If the conditions are otherwise unchanged, an increase in cloud condensation nucleii results in smaller cloud droplets, which itself results in a higher cloud reflectivity. Since aerosol particles also act as ice nucleii, they can initiate glaciation in liquid water and mixed phase clouds. Aerosol particles emitted into the atmosphere as a result of anthropogenic activity, which indirectly also includes emission changes due to changes in the climate system, have a negative effective radiative forcing (Forster et al. 2021). As already stated in the introduction, black carbon or soot aerosol are an exception, as they have a warming effect (Naik et al. 2021). When considering atmospheric feedbacks, like the ones sketched out here, soot is less warming, than estimated in the previous iteration of the Intergovernmental Panel's on Climate Change (IPCC) Assessment

Reports (Myhre et al. 2013), which mainly considered the instantaneous effects. The effects of aerosol-cloud interactions are not only limited to climate, but they also impact the strength of "medicanes", i.e. hurricane-like storms in the Mediterranean (Pravia-Sarabia et al. 2021). Mineral dust appears also to be linked to hurricane activity in the Atlantic Ocean (Evan et al. 2006).

By absorbing solar radiation aerosol particles also affect vegetation. Further, cations in aerosol particles also act as nutrients (Goudie 2009; Mahowald et al. 2017), which then impacts vegetation in both continental and marine ecosystems, including the Amazon rainforest (Bristow et al. 2010; Griffin and Kellogg 2004; Yu et al. 2015).

Highly absorbing aerosol, like black carbon/soot aerosol, deposited on highly reflective snow and ice surfaces, decreases the surfaces' albedo and by that influences the radiative balance (Bond et al. 2013).

The highly abrasive nature of volcanic ash can damage aircrafts, especially their wind shields, engines, and electronics, which means that aerosol particles also impact air traffic (Casadevall 1994). An increase in aerosol particle number decreases atmospheric visibility, i.e. the range at which a black object can be seen against the horizon (Seinfeld and Pandis 2016). Absorption and scattering by aerosol particles and molecules affects this range and the colouration of the sky. This change in atmospheric visibility can also affect (air) traffic. Heterogeneous chemical reactions can take place on surfaces areas provided by marine aerosol (Buseck and Pósfai 1999). Further, sea salt aerosol contribute to corrosion of metals and reinforced concrete structures in coastal areas (Meira et al. 2008).

Aerosols have also adverse impacts on human health. Specifically, they can contribute to and even cause cardiovascular, respiratory and allergic diseases (Pöschl 2005; Schmidt 2016). Wildfire smoke in particular was found to be linked to respiratory and cardiovascular symptoms, mortality, emergency rooms visits, inflammation markers and even lower birth weight (Liu et al. 2015b). Wildfire smoke is also a potential infectious agent, with infections potentially caused by co-emitted microbes (Kobziar and Thompson 2020). Microbes transported by dust storms similarly contribute to adverse effects on public health (Griffin and Kellogg 2004). Black carbon, which is an important part of wildfire smoke, is further associated with increased mortality from cardiopulmonary diseases and lung cancer (Anenberg et al. 2011; Anenberg et al. 2012). PM2.5 particles, i.e. particulate matter with a diameter smaller than 2.5 μm is linked with a decrease in fecundity and a higher probability of reduced fertility, as well as lowering ovarian reserve among women (Gaskins et al. 2019; Li et al. 2021).

Reducing soot emissions has co-benefits for both climate and air quality, and hence human health (Anenberg et al. 2012). However, sulphate aerosol has adverse effects on air quality (e.g. Anenberg et al. 2011), but a cooling effect on the climate (Naik et al. 2021).

Chapter 3

Remote sensing of atmospheric aerosol particles

Aerosol particles can be either observed by in situ measurements or by remote sensing techniques. Each method has its drawbacks and its advantages. In situ measurements allow for direct measurements of physical properties and chemical composition. However, they are limited in time and space. In addition, due to their very nature they disturb and potentially alter atmospheric aerosol. Remote sensing on the other hand provides information on unperturbed aerosol profiles, but physical and chemical information can only be inferred indirectly. Satellite-based remote sensing of aerosol particles allows for global observations and provides strong observational constraints on model representations of the global aerosol distribution (Lenoble et al. 2013).

Remote sensing techniques can, broadly speaking, be divided into two types: active and passive remote sensing. Passive remote sensing makes use of electromagnetic radiation emitted from an existing source, such as the Sun or stars, while in active remote sensing techniques electromagnetic radiation is emitted from an artificial source, e.g., by a laser. Both types of techniques are used to investigate aerosol particles. The focus in this thesis is placed on active remote sensing.

3.1 Passive remote sensing

Probably the most straightforward way for passive remote sensing of atmospheric aerosol particles is the measurement of the extinction related to aerosol.

The solar irradiance, which an instrument observes can be written as (Boucher 2015)

$$F(\lambda) = F_0(\lambda) \exp\left(-\tau(\lambda)\right). \tag{3.1}$$

In practice several measurements at different narrow spectral bands are taken, hence the dependency on the wavelength λ. F_0 is the solar irradiance at the top of the atmosphere and τ is the total extinction optical depth due to molecules, aerosol particles and clouds along the line of sight. To retrieve the aerosol related quantities observations contaminated with clouds are usually discarded. With the help of the

surface pressure the molecular extinction can be accounted for. Measurements at absorption lines of trace gases require further corrections. When approximating the atmosphere by a plane-parallel geometry, the optical depth along the path can be written as

$$\tau = (\tau_a + \tau_m)/\cos\theta_0. \tag{3.2}$$

with τ_a and τ_m being the vertical optical depth due to aerosols and molecules, respectively. θ_0 is the solar zenith angle.

From such observations the size distribution $n(r)$ can be obtained by inverting the following expression for the aerosol optical depth of a layer with thickness Δz under the assumption of homogeneous layer properties

$$\tau_a(\lambda) = \Delta z \int \pi r^2 Q_{\text{ext}}(r, \lambda, m) n(r) \mathrm{d}r. \tag{3.3}$$

Q_{ext} being the extinction efficiency as a function of radius r, wavelength λ and complex refractive index m. The complex refractive index describes the dielectric properties of the material, and depends on the chemical composition of the material.

Measuring $\tau_a(\lambda)$ at several wavelengths allows for an approximate aerosol size distribution to be inverted. However, its practical application is limited to radii smaller than 3 - 4 μm (Boucher 2015; King and Dubovik 2013). By observing scattered radiation this limitation can be overcome. The radiance scattered into a direction Θ can be expressed by

$$L(\lambda, \Theta) = \frac{\varpi(\lambda)\tau(\lambda)p(\lambda, \Theta)}{4\pi\cos\theta_0} F_0(\lambda). \tag{3.4}$$

With ϖ the single scattering albedo, a ratio of scattering and extinction efficiency, indicating how much radiation is scattered and how much absorbed, τ the optical depth and p the phase function of the molecules and aerosol particles. After correcting for effects from molecules, the aerosol phase function can be approximated from the measured radiance. Hence, the equation to be solved, thus becomes

$$p_{\text{aerosol}}(\lambda, \Theta) = \int p(\Theta, r, m) n(r) \mathrm{d}r. \tag{3.5}$$

By combining the observations of direct sun light (extinction measurements) and diffuse sun light (observation of scattered sun light), retrieval algorithms for sun photometers can obtain the aerosol size distribution and the single scattering albedo. For space-borne measurements surface contributions to the signal need to be taken into account.

For a more detailed, and mathematically more rigorous account of the inversion of passive aerosol observations, please refer to the discussions by King and Dubovik (2013).

3.2 Active remote sensing

Active remote sensing of aerosol particles is done by using lidar (light detection and ranging) instruments[1]. Lidar instruments emit short pulses of laser light at a single or at multiple specific wavelengths. The emitted radiation is transmitted and scattered or absorbed by cloud particles, aerosol particles and/or molecules. Part of the radiation is scattered in the direction of the receiver. Here a telescope collects all photons and an optical analysing system allows filtering for specific wavelengths and polarisation states. The focus here will be on monostatic lidar setups, for which transmitter and receiver are collocated. This allows inference range data by measuring the time between pulse emission and signal detection (Wandinger 2005).

In context of remote sensing of aerosol particles there are two main types of retrieval techniques (Ansmann and Müller 2005). The choice of these retrieval techniques is connected to the available lidar instrument. The first of these two techniques is connected to the measuring return signals by standard or elastic backscatter lidars. These lidar instruments detect the total atmospheric backscatter signal that means without separating the particle and the molecular contributions to the total backscatter. The extinction cannot be measured by these instruments, but has to be estimated from the backscatter profile. As a consequence elastic backscatter lidar instruments rely on making assumptions on the aerosol type. These instruments are not covered further here. For a brief discussion, including the relevant lidar equation, please see the discussion by Ansmann and Müller (2005). The profile of the particle extinction coefficient can, however, directly be determined by using the Raman lidar technique or the high spectral resolution lidar (HSRL) method. The backscatter coefficient is also obtained. Both Raman lidars and HSRLs allow for the separation of particle and molecular contributions of the backscattered signal. Another instrument type to obtain vertical profiles are scanning or multiangle lidars. Their main drawback is the requirement of horizontally homogeneous backscattering and extinction at all measurements heights. Often this requirement is not met in the boundary layer (Ansmann and Müller 2005).

Raman lidars measure both the return signals elastically backscattered by particles and molecules and the inelastically backscattered signal (a process called Raman scattering, hence the instrument's name) by nitrogen and/or oxygen molecules. The HSRL builds on the differences in the spectral line width of the elastically backscattered signal. Due to the much higher thermal motion of molecules, the corresponding line of the backscatter signal has experienced stronger Doppler-broadening, whereas, aerosol particles (and cloud particles) possess a much smaller thermal motion and therefore, their backscattering spectrum remains nearly unchanged. By using filters one channel can block out the narrow aerosol peak and detect only the signal pertaining to the molecules, and the other channel detects either the total signal or only the aerosol peak.

[1] A notable exception is the study by Klingebiel et al. (2019), which used a highly sensitive cloud radar measuring at 35.5 GHz (corresponds to $\lambda = 0.8$ cm), to detect hygroscopically grown sea salt aerosol particles. However, in general radar instruments are not sensitive enough for providing information on aerosol profiles. Hence, radar is not discussed further.

The lidar equation for the molecular backscatter signal $P(R, \lambda_{\mathrm{Ra}})$, measured by a monostatic lidar instrument with transmitted laser pulse energy E_0 and the instrument's characteristic efficiencies $\eta_{\lambda_{\mathrm{Ra}}}$, reads

$$P(R, \lambda_{\mathrm{Ra}}) = \frac{E_0 \eta_{\lambda_{\mathrm{Ra}}}}{R^2} O(R, \lambda_{\mathrm{Ra}}) \beta_{\mathrm{Ra}}(R, \lambda_0) \exp\left(- \int_0^R [\alpha(r, \lambda_0) + \alpha(r, \lambda_{\mathrm{Ra}})] \mathrm{d}r \right). \tag{3.6}$$

Here β_{Ra} describes, in case of an HSRL, Rayleigh backscattering; in case of Raman lidars it describes Raman backscattering. For non-overlap of the laser-beam and the receiver-field-of-view the overlap function $O(R, \lambda_{\mathrm{Ra}})$ needs to be considered. Extinction by particles is the only particle-scattering effect in this form of the lidar equation. $\alpha(R, \lambda_0)$ denotes the extinction along the way to the backscatter region, whereas, $\alpha(R, \lambda_{\mathrm{Ra}})$ denotes the extinction along the way back to the lidar instrument. In the Rayleigh case, as well as for rotational Raman backscattering it can be assumed that $\lambda_{\mathrm{Ra}} = \lambda_0$. For vibration-rotational Raman signals, the change of the wavelength needs to be considered. The molecular backscatter coefficient β_{Ra} can be calculated from the number density of air molecules, which itself can either be calculated from radiosonde measurements or from a standard atmosphere's profiles. From Eq. 3.6 and $\alpha = \alpha_{\mathrm{aer}} + \alpha_{\mathrm{mol}}$ the aerosol extinction coefficient α_{aer} can be obtained. Unlike the case of using the elastic backscatter lidar, no critical assumptions are needed. However, the lidar equation is based on the single-scattering approximation. Thus the main assumption is that multiple scattering effects within the detector's field of view can safely be neglected. From two more signal pairs of total and molecular backscatter, including measurements at a reference height in the upper troposphere with negligible particle scattering, the particle backscatter coefficient β_{aer} can be obtained.

Pulsed lasers used for lidar remote sensing produce linearly polarised light. Interaction of laser light with particles, including molecules, can change the polarisation state, i.e. the backscattered light may become depolarised (Sassen 2005). The combined depolarisation ratio from molecules and particles, called volume depolarisation ratio δ^v, can be obtained by measuring the parallel- ($P_\parallel$) and perpendicular-polarised ($P_\perp$) backscattered power or the corresponding backscattering coefficients (Freudenthaler et al. 2009)

$$\delta^v = \frac{P_\perp}{P_\parallel} = \frac{\beta_\perp}{\beta_\parallel}. \tag{3.7}$$

To disentangle the respective contributions the molecular depolarisation ratio needs to be determined

$$\delta^{\mathrm{mol}} = \frac{\beta_\perp^{\mathrm{mol}}}{\beta_\parallel^{\mathrm{mol}}}. \tag{3.8}$$

Depending on the measurement set-up the cross- and parallel-polarised particle backscatter coefficient may be available. In such a case the particle depolarisation ratio can be calculated analogous to Eq. (3.7). Should such measurements, however, not be available, the particle depolarisation ratio can be calculated using δ^v and δ^{mol}

(Freudenthaler et al. 2009)

$$\delta^{aer} = \frac{\beta_{\perp}^{\mathrm{aer}}}{\beta_{\parallel}^{\mathrm{aer}}} = \frac{(1+\delta^{\mathrm{mol}})\delta^{v}\mathbf{R} - (1+\delta^{v})\delta^{\mathrm{mol}}}{(1+\delta^{\mathrm{mol}})\mathbf{R} - (1+\delta^{v})}. \tag{3.9}$$

The backscatter ratio $\mathbf{R}$ is defined as

$$\mathbf{R} = \frac{\beta^{\mathrm{mol}} + \beta^{\mathrm{aer}}}{\beta^{\mathrm{mol}}}. \tag{3.10}$$

Since the linear depolarisation ratio in backscattering direction is identically to zero for homogeneous spheres (and other spherically symmetric, but inhomogeneous particles), its measurements and the interpretation allow discerning particle shapes.

3.3 Inferring microphysical aerosol properties from remote sensing

Both passive and active remote sensing techniques and combinations thereof aim at retrieving aerosol microphysical properties. Ansmann and Müller (2005) classify retrieval methods for lidar measurements into three different, distinct groups. The first group contains combinations of (monostatic) lidar instruments with other instruments. These instruments can be in-situ measurements. Applications are usually limited to specific field campaigns, but provide detailed knowledge of microphysical aerosol properties. Another type of instruments would be sun photometers, which provide retrieved particle size distributions and an estimate of the aerosol complex refractive index. Both types of instruments, however, require the observation of the same particle volume by the lidar and the auxiliary instrument. The second group of retrieval methods relies on Mie-scattering calculations, intended to reconstruct the backscattering coefficient derived from lidar observations. The aerosol complex refractive index and the particle size distribution would here be assumed a priori. Due to the use of Mie-scattering calculations spherical particle shapes are implicitely assumed. The uncertainties associated with this approach restrict the practical application of this method. It has successfully been used for remote sensing of stratospheric particles, which are less diverse than tropospheric aerosol. This method also allows for a coarse classification of tropospheric aerosol particles (Ansmann and Müller 2005; Post et al. 1996; Sasano and Browell 1989). The third and last class combines mathematical tools with multiwavelength lidar measurements. It makes use of spectral information in backscatter and extinction measurements and the dependence on particle size. Compared to the previous class less a priori information is required. Thus we do not have to make assumptions about the particle volume, the specific form of the size distribution, or the complex refractive index (Böckmann 2001; Müller et al. 1999). The combination of technically robust multiwavelength measurements of extinction and backscatter and the mathematical tools used make the inversion methods both versatile and robust for highly variable tropospheric aerosol (Ansmann and Müller 2005; Böckmann 2001).

This third class is the standard approach for microphysical retrievals and referred to as regularisation with constraints. The optical properties are related to the microphysical properties by Fredholm integral equations of the first kind[2]

$$g_p = \int_{r_{min}}^{r_{max}} K_p(r, m) v(r) \mathrm{d}r + \epsilon_p^{\mathrm{exp}}. \tag{3.11}$$

The optical data is denoted as g. K stands for the Kernel efficiencies, which are a function of radius r and complex refractive index m. The data has an error ϵ. $v(r)$ is the particle volume concentration per size interval $\mathrm{d}r$. The subscript p denotes both the kind of data (i.e., extinction coefficient, backscatter coefficient) and the wavelength. The radii r_{min} and r_{max} are defined by the range at which particles contribute to the signal. Below r_{min} the particles are no longer optically efficient. For example for a wavelength of $\lambda = 355\,\mathrm{nm}$ the lower bound would be at $r_{\mathrm{min}} \approx 50\,\mathrm{nm}$. The upper bound r_{max} is defined by the particle size, at which concentrations are so low that particles no longer significantly contribute to the signal. For tropospheric aerosol this is typically below $10\,\mu\mathrm{m}$.

Retrieving microphysical properties from lidar measurements requires solving an ill-posed problem. Various factors contribute to this classification. Tropospheric aerosol is highly complex, as the discussion in Sec. 2.2 indicated. The number of variables required for unambiguous characterisation of the aerosol particles is typically higher, than the number of independent observed quantities. This causes the mathematical problem to have a non-unique solution. Different combinations of particle shape, size, complex refractive index, and size distribution can lead to similar optical properties, which are no longer distinguishable within the margin of error. The large range of values of matrix elements in the matrix formulation of Eq. 3.11 can result in a non-continuous dependence of the solution on the input data.

A numerical solution to Eq. 3.11 can be obtained after rewriting the equation as a matrix equation. A mathematical procedure called regularisation is used to avoid error amplification and the solution becoming non-unique. With this procedure solutions are calculated for which the error term drops below a predefined threshold value. In this minimisation process a penalty term is included, which contains physical constraints to the solution. A more detailed account of this method was provided by Ansmann and Müller (2005).

For particle characterisation, i.e. the retrieval of complex refractive index, effective radius, and volume, surface area, and number concentrations, measurements at at least three different wavelengths are required. By using backscattering coefficients measured at up to six wavelengths the accuracy of the results can be increased. If measurements of the linear depolarisation ratio are included in the retrieval process non-spherical geometries can be accounted for.

Measurements of the backscattering coefficient at three wavelengths and of the extinction coefficient at two wavelengths are routinely provided by modern lidar instruments. Such a system is referred to as $3\beta{+}2\alpha$ system. Adding the depolarisation ratio at one wavelength consequently results in a $3\beta{+}2\alpha{+}1\delta$ system. Such an addition

[2]The inversion of passive remote sensing measurements uses Fredholm integral equations, too (King and Dubovik 2013).

allows the retrieval of shape information (Ansmann and Müller 2005), as well as for the optical partitioning of two and three component particle mixtures (Miffre 2015; Tesche et al. 2009; Veselovskii et al. 2018). Raman lidars and HSRL commonly use Nd:YAG (neodymium-doped yttrium-aluminium garnet) lasers (Eloranta 2005; Wandinger 2005). Thus, the wavelengths in question are typically 355 nm, 532 nm, and 1064 nm. Lidar measurements of the extinction coefficient at 1064 nm have only become possible in the recent years (Haarig et al. 2018, 2016). A recent study by Tesche et al. (2019) recommends the use of linear depolarisation ratio measurements at 355 nm, and if possible, also at 532 nm for microphysical aerosol retrievals.

Chapter 4

Radiative transfer and single scattering properties

The physical conceptualisation of remote sensing relies on a description of the energy transport in form of electromagnetic radiation in the atmosphere, i.e. radiative transfer. As briefly mentioned in the previous chapter, the interpretation of remote sensing observations builds upon computations of single scattering properties, which are linked to interactions of electromagnetic waves. This chapter introduces the fundamentals of radiative transfer theory. The basic terminology of the radiometric quantities and the single scattering properties is introduced.

4.1 Atmospheric radiative transfer

The transport of electromagnetic radiation through the atmosphere is referred to as atmospheric radiative transfer. Applications of radiative transfer include remote sensing, temperature forecasting, or energy balance calculations.

Figure 4.1 shows the solar spectrum at the top of the atmosphere (TOA) in grey and the spectrum at the Earth's surface in black. Both curves are shown as a function of wavelength. Differences between the two spectra can be attributed to molecular absorption by O_3, CO_2, H_2O, and O_2. The dotted vertical lines indicate the different spectral ranges, ultraviolet (UV) for wavelengths up to 400 nm, visible light (VIS), and infrared radiation (IR) from wavelengths of 760 nm (Zdunkowski et al. 2007). Electromagnetic radiation with wavelengths below 10 nm, is classified as X-rays and gamma radiation. However, the solar emissions at these wavelengths is negligible when it comes to atmospheric radiative transfer. The infrared spectral band extends further to a wavelength of up to 1 mm, although only about 0.9% of the solar power output is emitted at wavelengths larger than 4 μm (Petty 2006).

Radiative transfer can be quantitatively described using the radiative transfer equation. Its standard form for a three-dimensional medium as given by e.g., Zdunkowski et al. (2007) is

$$-\frac{1}{k_{\text{ext},\nu}}\Omega\nabla I_\nu = I_\nu - \frac{\varpi_{0,\nu}}{4\pi}\int_{4\pi} p(\Omega'\cdot\Omega)I_\nu(\Omega')\mathrm{d}\Omega' - \frac{1}{k_{\text{ext},\nu}}J^e_\nu. \tag{4.1}$$

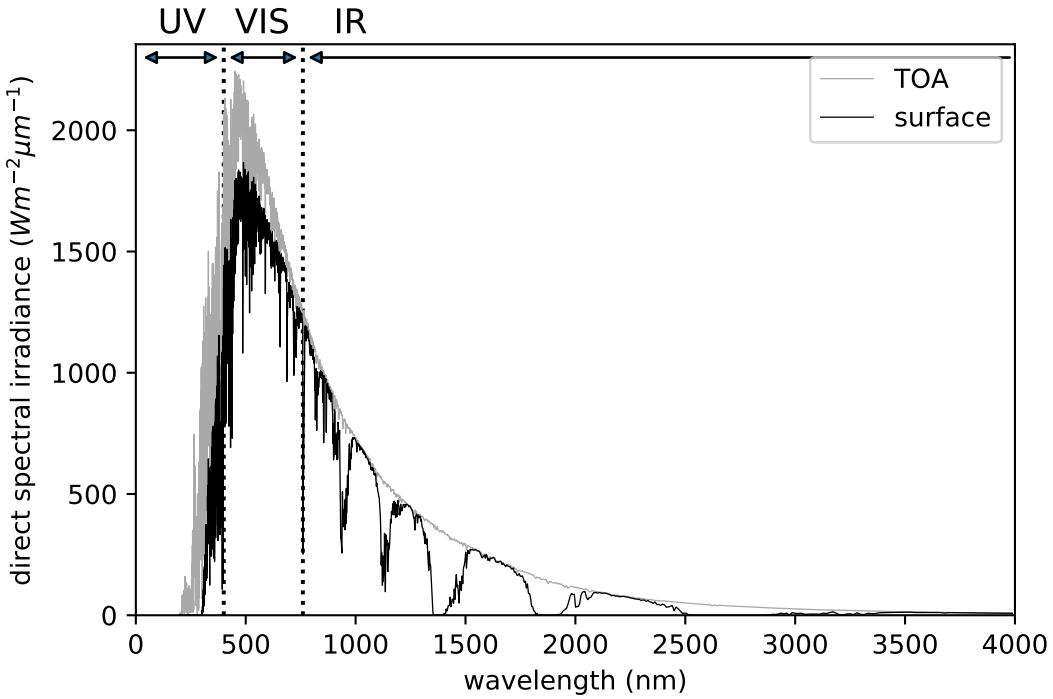

Figure 4.1: Solar spectrum as a function of wavelength at the top of atmosphere (TOA, grey) and at the surface (black), dotted lines indicate spectral ranges of ultraviolet (UV), visible (VIS), and infrared (IR) radiation. The spectra were calculated with the radiative transfer software package libRadtran (Emde et al. 2016; Mayer and Kylling 2005) using the discrete ordinate radiative transfer solver DISORT and the parametrised bands and channels for molecular absorption called REPTRAN (Gasteiger et al. 2014).

The radiative transfer equation is a integro-differential equation and describes sources and sinks of electromagnetic radiation, travelling through a medium, here the atmosphere. Electromagnetic radiation is quantified by the spectral radiance I_ν. Losses of radiation by absorption or scattering out of the direction of propagation Ω, i.e. extinction of radiation, are described by the first term $-\frac{1}{k_{\text{ext},\nu}}\Omega\nabla I_\nu$. k_{ext} is the volumetric or bulk extinction coefficient, which quantifies the extinction. The direction of propagation Ω is mathematically described by a unit vector. The second term, $-\frac{\varpi_{0,\nu}}{4\pi}\int_{4\pi} p(\Omega'\cdot\Omega)I_\nu(\Omega')\mathrm{d}\Omega'$, describes radiation scattered into the direction of propagation. The phase function p describes the angular distribution of scattered radiation. $\Omega'\cdot\Omega$ denotes the cosine of the scattering angle ϑ and $\varpi_{0,\nu}$ the bulk single scattering albedo. The emission of electromagnetic radiation is described by $-\frac{1}{k_{\text{ext},\nu}}J^e_\nu$. In the troposphere and stratosphere the emission source term is proportional to the Planck function, i.e., there are conditions of local thermodynamic equilibrium. However, it should also be stressed that in the solar radiation's main spectral range (for wavelengths below $4\,\mu$m) the emission source term can be neglected.

A microphysical derivation of the radiative transfer equation, which links it back to the scattering problem and Maxwell's equations (see Section 4.2) and requires

only a limited number of assumptions is presented by Mishchenko et al. (2006)[1]. The elastic lidar equation, mentioned in Sec. 3.2 can be derived from the radiative transfer equation, as shown by Ceolato et al. (2020).

Integro-differential equations, such as the radiative transfer equation, are difficult to solve. There are different techniques to solve it, as for example discussed by Zdunkowski et al. (2007). The respective choice of solving technique depends on the intended application. As is evident from Eq. 4.1 the radiative transfer equation is linked to single scattering properties.

4.2 Single scattering properties

At a given point the electromagnetic state of matter is described by the volume density charge ρ, the volume density of electric dipoles or polarisation P, the volume density of magnetic dipoles or magenetisation M, and the electric current per unit area or current density J. These quantities are linked to the electric fields $\vec{E}$ and magnetic fields $\vec{H}$ by Maxwell's equations, which form the basis of the theory of classical optics phenomena (e.g. Mishchenko et al. 2006; Zdunkowski et al. 2007). The electric displacement can be defined as $\vec{D} = \epsilon_0\vec{E} + \vec{P}$ and the magnetic induction as $\vec{B} = \mu_0(\vec{H} + \vec{M})$ with ϵ_0 and μ_0 being the permittivity and the permeability in vacuum, respectively. Permittivity and permeability are measuring how a material responds to an electric and a magnetic field. Thus, Maxwell's equations can be written as

$$\nabla \cdot \vec{D} = \rho \qquad \nabla \cdot \vec{B} = 0 \tag{4.2}$$

$$\nabla \times \vec{E} = \frac{\partial \vec{B}}{\partial t} \qquad \nabla \times \vec{H} = \vec{J} + \frac{\partial \vec{D}}{\partial t}. \tag{4.3}$$

The current density of the conduction electrons in response to the electric field is denoted by $\vec{J} = \sigma\vec{E}$, with σ being the electrical conductivity. Maxwell's equations are often solved in the frequency domain, because then the constitutive relations for linear, isotropic materials are given by the simple linear relations $\vec{D} = \epsilon\vec{E}$ and $\vec{B} = \mu\vec{H}$. Analogous to ϵ_0 and μ_0, ϵ and μ are the permittivity and permeability, respectively, and are material constants.

Propagation of electromagnetic radiation in an homogeneous, source-free medium, can be described by plane electromagnetic waves (e.g., Mishchenko et al. 2002), which are solutions to Maxwell's equations (Fleisch 2019)

$$\vec{E} = \vec{E}_0 \exp\left(-\vec{k}_I \cdot \vec{r}\right) \exp\left(i\vec{k}_R \cdot \vec{r} - i\omega t\right), \tag{4.4}$$

[1]The radiative transfer equation as defined by Zdunkowski et al. (2007) and as given here assumes the atmosphere to be an isotropic medium, while Mishchenko et al. (2006) state the radiative transfer equation for a more general case of an anisotropic medium. Hence, Mishchenko et al. (2006) introduce the extinction matrix, which takes the directional dependence of the extinction in case of anisotropy into account. However, for all practical purposes the atmosphere can be considered an isotropic medium (Zdunkowski et al. 2007).

$$\vec{H} = \vec{H}_0 \exp\left(-\vec{k}_I \cdot \vec{r}\right) \exp\left(i\vec{k}_R \cdot \vec{r} - i\omega t\right). \tag{4.5}$$

$\vec{E}$ and $\vec{H}$ denote the electric and the magnetic field vector. $\vec{k}_I$ and $\vec{k}_R$ denote the imaginary and the real part of the complex wave vector. Thus, the amplitudes of the electric and the magnetic waves are described by $\vec{E}_0 \exp\left(-\vec{k}_I \cdot \vec{r}\right)$ and $\vec{H}_0 \exp\left(-\vec{k}_I \cdot \vec{r}\right)$, respectively. $i\vec{k}_R \cdot \vec{r} - i\omega t$ denotes the waves' phase. The electromagnetic energy flow is described in magnitude and direction by the Poynting vector. The Poynting vector of a plane wave is (Mishchenko et al. 2002)

$$S(r) = \frac{1}{2}[E(r) \times H^*(r)]. \tag{4.6}$$

So far the propagation of plane waves in an unbound medium were considered. In the presence of a particle the electromagnetic field changes. To easily observe these changes induced by particles in a non-absorbing medium, further quantities of the particle need to be introduced. The time averaged Poynting vector is the Poynting vector's real part and can be decomposed into an incident, scattered and extinct component, when considering the scattering problem

$$\langle S(r)\rangle = Re(S(r)) = \langle S^{\text{inc}}(r)\rangle + \langle S^{\text{sca}}(r)\rangle + \langle S^{\text{ext}}(r)\rangle. \tag{4.7}$$

Here $\langle S^{\text{inc}}(r)\rangle$ and $\langle S^{\text{sca}}(r)\rangle$ are the (time-averaged) Poynting vectors of the incident and the scattered field, respectively. $\langle S^{\text{ext}}(r)\rangle$ can be seen as caused by the interaction of the incident and the scattered field.

With the help of the time averaged Poynting vector, the optical cross sections of a scatterer in a non-absorbing medium can be determined, by surrounding the scatterer with an imaginary sphere with a surface area A. The net rate at which electromagnetic energy crosses the surface A is equal to the power the particle absorbs,

$$W^{\text{abs}} = -\int_A \langle S(r)\rangle \hat{r} \mathrm{d}A. \tag{4.8}$$

The extinct power W^{ext} and the scattered W^{sca} can be calculated analogously. W^{inc}, which is suggested by Eq. 4.7 vanishes, since the surrounding medium is considered to be non-absorbing. W^{sca} is the rate at which the imaginary sphere's surface is crossed in the outward direction,

$$W^{\text{sca}} = \int_A \langle S^{\text{sca}}(r)\rangle \hat{r} \mathrm{d}A. \tag{4.9}$$

W^{ext} is equal to the sum of the energy scattering rate and the energy absorption rate

$$W^{\text{ext}} = W^{\text{sca}} + W^{\text{abs}} = -\int_A \langle S^{\text{ext}}(r)\rangle \hat{r} \mathrm{d}A. \tag{4.10}$$

With the help of these expressions the optical cross sections can finally be calculated by

$$C_{\text{ext}} = \frac{W^{\text{ext}}}{\frac{1}{2}\sqrt{\frac{\epsilon_1}{\mu_0}}|E_0^{\text{inc}}|^2} \tag{4.11}$$

and

$$C_{\mathrm{sca}} = \frac{W^{\mathrm{sca}}}{\frac{1}{2}\sqrt{\frac{\epsilon_1}{\mu_0}}|E_0^{\mathrm{inc}}|^2} \tag{4.12}$$

and C_{abs} can be calculated as

$$C_{\mathrm{abs}} = C_{\mathrm{ext}} - C_{\mathrm{sca}}. \tag{4.13}$$

The extinction cross section is, in fact, an observable quantity, and the optical cross sections have units of area.

The ratio of scattering and extinction cross section, which was already introduced in Sec. 3.1, is commonly referred to as single scattering albedo ϖ or SSA

$$\varpi = \frac{C_{\mathrm{sca}}}{C_{\mathrm{ext}}}. \tag{4.14}$$

For a purely scattering medium the SSA takes a value of 1, since for this case $C_{\mathrm{ext}} = C_{\mathrm{sca}}$, while for a purely absorbing medium the SSA is equal to 0.

Electromagnetic radiation can be described by the Stokes vector[2] (I, Q, U, V), which quantifies the magnitude I and the polarisation Q, U, V. Q denotes the linear polarisation with respect to a reference plane through the direction of propagation, U the linear polarisation with respect to a plane tilted by $\pm 45°$ compared to the polarisation plane, and V the circular polarisation.

The scattered Stokes vector $(I_{\mathrm{sca}}, Q_{\mathrm{sca}}, U_{\mathrm{sca}}, V_{\mathrm{sca}})$ can be related to the incident Stokes vector $(I_{\mathrm{inc}}, Q_{\mathrm{inc}}, U_{\mathrm{inc}}, V_{\mathrm{inc}})$ with the help of the scattering matrix S. In case of totally random orientation of scatterer with a plane of symmetry (or a mirror-symmetric counterpart present) either scatterer would constitute a macroscopic isotropic and mirror-symmetric medium[3]. Hence, the relationship can be expressed as (Hulst 1981; Mishchenko et al. 2002)

$$\begin{pmatrix} I_{\mathrm{inc}} \\ Q_{\mathrm{inc}} \\ U_{\mathrm{inc}} \\ V_{\mathrm{inc}} \end{pmatrix} = \frac{1}{k^2 r^2} \begin{pmatrix} S_{11} & S_{12} & 0 & 0 \\ S_{12} & S_{22} & 0 & 0 \\ 0 & 0 & S_{33} & S_{34} \\ 0 & 0 & -S_{34} & S_{44} \end{pmatrix} \begin{pmatrix} I_{\mathrm{sca}} \\ Q_{\mathrm{sca}} \\ U_{\mathrm{sca}} \\ V_{\mathrm{sca}} \end{pmatrix}. \tag{4.15}$$

A macroscopically isotropic and mirror-symmetric scattering medium appears to be a rather special case, however, in practice it provides a very good numerical description of different particles, including fractal aggregates, which are discussed in more detail in Chapter 5 (Ceolato et al. 2020; Mishchenko et al. 2002). In case of unpolarised incident radiation, i.e. radiation with a Stokes vector of $(I_{\mathrm{inc}}, 0, 0, 0)$, the $S_{1,1}$ element describes the angular distribution of scattered intensity. It is also referred to as scattering phase function p. The scattering matrix in Eq. 4.15 is

[2]The literature is not consistent, whether the Stokes vector is defined as a generalised form of the radiance (Mishchenko et al. 2002) or as a generalisation of irradiance (Bohren and Huffman 1983). A middle way was chosen by Zdunkowski et al. (2007), who defined the Stokes vector elements loosely as intensities with different possible units. As a consequence Zdunkowski et al. (2007) introduced conversions factors, carrying the units required for the intended definition.

[3]This would not apply to, for example, left- or right-handed helices as scatterers.

defined, so that $\int_{4\pi} p\mathrm{d}\Omega = C_{\mathrm{sca}}$. Commonly the scattering matrix is normalised, so that $\int_{4\pi} p\mathrm{d}\Omega = 1$. In case of such a normalisation the matrix is then referred to as (normalised) Stokes matrix F.

From the scattering matrix elements more quantities can be calculated. Among these quantities is the asymmetry parameter g or ASY, which can be calculated by

$$g = ASY = \int_{4\pi} F_{11} \cos\vartheta \mathrm{d}\Omega \tag{4.16}$$

The asymmetry parameter describes the dominant scattering direction. The asymmetry parameter is $g = 0$ for isotropic scattering, which means that the same amount is scattered in all directions, or if the scattering is symmetric about a scattering angle of 90°, such as Rayleigh scattering[4]. In case forward scattering dominates, $g > 0$ and if the backward scattering dominates, $g < 0$ (Bohren and Huffman 1983; Mishchenko et al. 2002).

Quantities routinely measured by lidar instruments include the extinction coefficient, the backscattering coefficient, the extinction-to-backscatter ratio and the linear depolarisation ratio (see Sec. 3.2). These quantities can also be calculated from the optical cross sections and the scattering matrix elements. The size-averaged (aerosol) extinction coefficient α between the lower limit of the size distribution r_{min} and the upper limit r_{max} can be calculated from the extinction cross section and the size distribution by (Gasteiger et al. 2011)

$$\alpha = \int_{r_{\mathrm{min}}}^{r_{\mathrm{max}}} C_{\mathrm{ext}}(r) n(r) \mathrm{d}r. \tag{4.17}$$

The size-averaged backscatter coefficient β is defined as

$$\beta = \int_{r_{\mathrm{min}}}^{r_{\mathrm{max}}} \frac{C_{\mathrm{sca}}(r) F_{11}(r, 180°) n(r)}{4\pi} \mathrm{d}r. \tag{4.18}$$

Here F_{11} is the (1,1)-element of the normalised Stokes matrix F and C_{sca} the scattering cross section, as defined above. The product of $F_{11}(180°)$ and C_{sca} is also referred to as the backscattering cross section C_{bsc}. It quantifies the amount of radiation scattered backwards.

The size-averaged extinction-to-backscatter ratio S_p, or as it is especially in the context of lidar remote sensing often called, lidar ratio, can then be calculated by

$$S_p = \frac{\alpha}{\beta}. \tag{4.19}$$

While both α and β depend on the total particle number, S_p is independent of the particle number. For individual particles $S_p(r)$ can be calculated by

$$S_p(r) = 4\pi \frac{C_{\mathrm{ext}}(r)}{C_{\mathrm{sca}}(r) F_{11}(r, 180°)}. \tag{4.20}$$

[4]In some cases in the literature, such as for example by Davies and Knyazikhin (2010) isotropic scattering is (implicitly) defined as scattering with $g = 0$.

In case a lidar instrument operates at multiple wavelengths, spectral changes of the measured quantities can be observed. The spectral change of a quantity x between two wavelengths λ_1 and λ_2 ($\lambda_1 < \lambda_2$) is expressed by the Ångström exponent

$$\text{å}_{\text{x},\lambda_1,\lambda_2} = \frac{\ln(x_1/x_2)}{\ln(\lambda_2/\lambda_1)} \tag{4.21}$$

x can be extinction coefficient α, backscattering coefficient β, or the extinction-to-backscatter ratio S_p. The Ångström exponents[5] are related by $\text{å}_{\alpha,\lambda_1,\lambda_2} = \text{å}_{\beta,\lambda_1,\lambda_2} + \text{å}_{\text{S},\lambda_1,\lambda_2}$ (Ansmann et al. 2002).

The polarisation state of electromagnetic radiation can change due to interaction with particles. Remote sensing techniques use in case of lidar linearly polarised light emitted from lasers. This polarised light can become depolarised. The depolarisation is expressed in the linear depolarisation ratio, which is the ratio between the light polarised perpendicularly and the light polarised parallel to the scattering plane. From the (11), (12), and (22) scattering matrix elements the linear depolarisation ratio can be calculated (Schnaiter et al. 2012; Takano and Jayaweera 1985)

$$\delta_l = \frac{S_{11} - S_{22}}{S_{11} \pm 2S_{12} + S_{22}}. \tag{4.22}$$

The $\pm 2S_{12}$ term's sign is determined by the incident polarisation; the plus sign is to be used for parallel incident laser polarisation and the minus sign for perpendicular incident laser polarisation. In backscattering direction, i.e. $\vartheta = 180°$, the (12) element is $S_{12} = 0$. Hence, the backscattering depolarisation ratio is independent of the incident light's polarisation and can be calculated by (Mishchenko and Hovenier 1995)

$$\delta_l = \frac{S_{11} - S_{22}}{S_{11} + S_{22}}. \tag{4.23}$$

The linear depolarisation ratio takes values between 0 and 1. The size-averaged depolarisation ratio, which can be compared to the particle linear depolarisation ratio δ_l^{par}, as measured by lidar instruments (see Sec. 3.2), can be obtained from the size-averaged matrix elements. For spherical rotationally symmetric particles, such as homogeneous spheres or centred core-shell geometries, $S_{11} = S_{22}$. Consequently, δ_l is identically to zero. Non-zero values indicate deviations of the scatterer from spherical symmetry. This deviations may be in shape and/or composition. However, it should be noted that there is not necessarily a monotonic connection between the scatterer's sphericity and the associated linear depolarisation ratio (e.g., Bi et al. 2018a). Provided the scatterer is in the right size range, the largest values of δ_l may be observed for mildly non-spherical shapes.

[5]There is another definition of the Ångström exponent, with the denominator being $\ln(\lambda_1/\lambda_2)$ (e.g. Janicka and Stachlewska 2019). The resulting values obtained from these two versions of the Ångström exponent differ only in sign.

4.3 Single scattering solvers

The scattering matrix S as defined in Eq. 4.15 can be obtained using various numerical techniques. Mie (1908) proposed a mathematically rigorous description of the scattering of plane waves by homogeneous spheres. These formulas are an exact solution to Maxwell's equations and form the basis of what is now referred to as Mie theory (Hergert and Wriedt 2012). Modifications allow for the application of other geometries to the Mie theory, such as concentric core-shell geometries, i.e. a sphere with a spherical hull, spheres in an absorbing medium or magnetic spheres. In case of particles much smaller than the incident wavelength, i.e. particles with a size parameter of $x = 2\pi r_{\text{eff}}/\lambda \ll 1$, Rayleigh scattering can approximate the Mie solution sufficiently well. Geometric optics, on the other hand, are a suitable approximation for particle much larger than the incident wavelength ($x \gg 1$) (Bohren and Huffman 1983).

Non-spherical particles, such as various different aerosol particles, require different methods, an overview can be found in the tutorial paper by Kahnert (2016). Here, two methods will be introduced briefly. Waterman (1965) proposed the T-matrix method, which provides highly accurate results. The T-matrix is dependent on the refractive index, the wavelength and the particle's size and shape, but it is independent on the incident field's direction. A main advantage is that orientation averaging is performed analytically. The required computation time can be drastically reduced by symmetries, especially axial symmetries (Kahnert 2016). If particles consisting of multiple spheres with non-intersecting surfaces are treated with a T-matrix formalism, it can be considered as an extension of Mie theory (Hergert and Wriedt 2012).

The discrete dipole approximation (DDA) divides the scatterer into small, fully polarisable volume elements to solve the volumetric scattering equation. The method was proposed by Purcell and Pennypacker (1973) and later refined by Draine and Flatau (1994). The volume elements, so called dipoles, are smaller than the wavelength and interact with each other and the incident field. As a result of this a set of linear equations can be obtained, which can be solved using standard numerical methods. In contrast to the T-matrix method, the solution depends on the incident field. Since the scatterer is divided into small volume elements arbitrary shapes can be treated. Furthermore, arbitrary inhomogeneities within a particle can be considered, since the complex refractive index is associated to the polarisability of each dipole individually. A more in-depth discussion of the DDA is provided by Yurkin and Hoekstra (2007, 2011). The accuracy of and the required computation time for the DDA result depends on the coarseness of the dipole spacing and the number of angles considered for orientation averaging.

The choice of the single scattering solver, the optical quantities of interest and the choice of the particle model are usually linked. Mie codes require spherical shapes. Waterman's T-matrix method can be used for particle models with a known surface parametrisation in spherical coordinates (the use of symmetric shapes is computationally especially advantageous). Modifications of the T-matrix method allow treatment of inhomogeneous particles (Mackowski and Mishchenko 1996; Quirantes 2005) and particles without a surface parametrisation in spherical coordinates (Mackowski and

Mishchenko 1996). The DDA can be employed for arbitrarily shaped particles, but usually at higher computational cost.

Chapter 5

Particle models

In order to calculate radiometric and polarimetric quantities of aerosol particles different particle models can be employed. Integral scattering properties, such as the extinction, absorption and scattering cross sections, required less morphological details than differential optical properties like the linear depolarisation ratio or the backscattering cross section (Kahnert et al. 2013). As a rule of thumb, the computational demand increases with increasing complexity of the particle models. As a consequence particle models require simplifications to be used in large scale applications like climate modelling or remote sensing retrievals (Kahnert et al. 2014). The focus here is on particle models used for soot (or black carbon), mineral dust, and sea salt aerosol.

5.1 Black carbon/soot

Black carbon or soot particles are formed during combustion processes in flames. According to Bond et al. (2013) they are characterised by four physical properties. Soot particles are strongly light absorbing, retain the basic form at high temperatures (i.e., are refractory), are water-insoluble, and exist as aggregates of small carbonaceous spherules.

5.1.1 Bare soot

The morphology of bare aggregates is commonly described by a model in which N spherical monomers of radius a are assembled into a fractal aggregate. These aggregates follow a fractal scaling relation (Sorensen 2001)

$$N = k_0 \left(\frac{R_g}{a} \right)^{D_f}. \tag{5.1}$$

Here k_0 is a fractal prefactor, describing how densely the monomers along an existing branch are packed. D_f, the fractal dimension, quantifies the compactness of an aggregate with values between 1, corresponding to linearly aligned monomers, and 3, corresponding to a sphere. Laboratory measurements by Xiong and Friedlander (2001) suggest that for soot aggregates a range of $1.5 \leq D_f \leq 3.0$ is expected. The

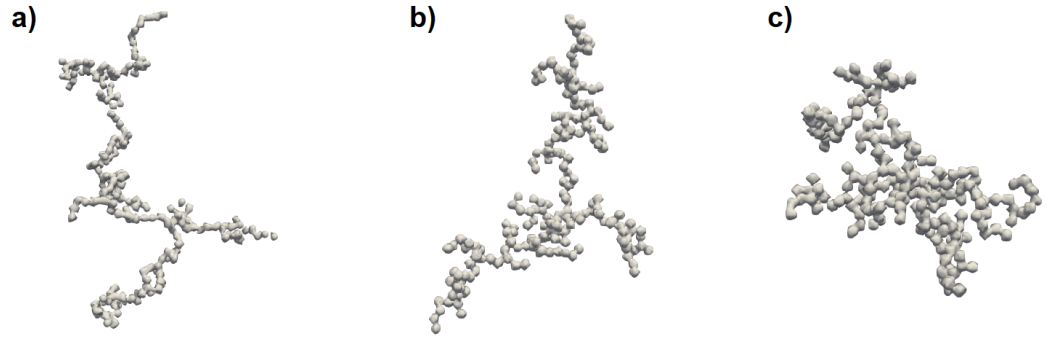

Figure 5.1: Example geometries for bare aggregates with $N = 216$. The fractal parameters shown are $k_0 = 0.7$, $D_f = 1.8$ (a), $k_0 = 1.1$, $D_f = 1.8$ (b), and $k_0 = 0.7$, $D_f = 2.2$ (c). All aggregates were obtained using an aggregation algorithm.

values of D_f depend on the fuel type and the combustion conditions (Bond and Bergstrom 2006; Xiong and Friedlander 2001). The overall aggregate size is denoted by the radius of gyration R_g, which is usually defined as (Sorensen 2001)

$$R_g = \sqrt{\frac{1}{N}\sum_{i=1}^{N} |\vec{r}_i - \vec{r}_c|^2}. \tag{5.2}$$

The distance between the ith monomer and the aggregate's centre of mass is $|\vec{r}_i - \vec{r}_c|$. Implicitly Eq. 5.2 assumes that the individual monomers are of same mass. To account for different monomer masses m_i, the radius of gyration has to be defined as (Eggersdorfer and Pratsinis 2012)

$$R_g = \sqrt{\frac{\sum_{i=1^N} |\vec{r}_i - \vec{r}_c|^2 m_i}{\sum_{i=1}^{N} m_i}}. \tag{5.3}$$

Should monomers within an aggregate have different masses, they are usually polydisperse. To account for polydispersity the monomer radius a in Eq. 5.1 needs to be replace with the monomers' geometric mean radius (Eggersdorfer and Pratsinis 2012).

Example geometries for aggregates consisting of $N = 216$ monomers are shown in Fig. 5.1. From left to right the fractal parameters are as follows: $k_0 = 0.7$, $D_f = 1.8$ (a), $k_0 = 1.1$, $D_f = 1.8$ (b), and $k_0 = 0.7$, $D_f = 2.2$ (c). Fig. 5.1 illustrates the increased packing density of monomers along a branch with increasing k_0 ((a) and (b)), as well as the aggregate's increasing compactness with increasing D_f ((a) and (c)). The example aggregates were constructed using the aggregation algorithm by Mackowski (2006). This algorithm starts constructing aggregates by randomly joining two monomers; in this initial step Eq. 5.1 is usually not fulfilled. The aggregate grows step-by-step by adding smaller aggregates and individual monomers to it, such that that the fractal scaling relation (Eq. 5.1) is satisfied at each individual step until the predefined number of monomers N is reached.

Differences in aggregate shape and composition, represented by fractal dimension and refractive index, impact optical properties, such as the optical cross sections

and the asymmetry parameter, as was investigated by Liu et al. (2008). Ceolato et al. (2020) proposed superaggregates, which are larger than "standard" aggregates. These superaggregates display a similar spectral behaviour and result in optical cross section and linear depolarisation ratio, which are larger than for the smaller "standard" aggregates. Laboratory studies indicate that fractal aggregates consist of polydisperse monomers. Doner and Liu (2017) and Liu et al. (2015a) studied the impact of polydisperse monomers compared to more simplified aggregates with monodisperse monomers. They found that polydispersity enhances differential optical cross sections (Doner and Liu 2017) and the scattering cross section, while only introducing insignificant changes in the scattering matrix elements (Liu et al. 2015a).

Fractal aggregates, which are constructed following the fractal scaling relation in Eq. 5.1, result in aggregates with monomers in point-contact, i.e. the neighbouring monomers share only a single point. Physical processes, such as coagulation, during aggregate formation are reflected by monomers in point-contact. The contact between two neighbouring monomers can increase by chemical sintering (Brasil et al. 1999; Eggersdorfer and Pratsinis 2012). This can be represented by overlapping monomers. Overlapping monomers and the effects on optical properties were investigated by Doner and Liu (2017), Doner et al. (2017), Skorupski and Mroczka (2014), and Yon et al. (2015). Overlapping decreases optical cross sections in the UV, but increases them at longer wavelengths.

Teng et al. (2019) provided a detailed study of deviations from an idealised monodisperse fractal aggregates and their impact on optical cross sections, single scattering albedo, and asymmetry parameter. In addition to polydispersity and overlapping monomers, these deviations also include a very thin non-absorbing coating, monomer surface irregularities, and necking. Necking refers to the process of adding additional material between two neighbouring monomers to smoothen the transition. Of these deviations from an idealised fractal aggregate the increase in particle mass by necking was found to have the largest impact. With a rather simple scaling relation with the volume changes and multiplication with an empirical factor of 1.05 these deviations in scattering and absorption cross section can be accounted for. The scattering matrix elements and the asymmetry parameter show only negligible changes caused by these deviations from ideal shape. Thus, they require no further correction.

5.1.2 Coated soot

Atmospheric soot aerosol particles are commonly internally mixed with or coated by non-absorbing or weakly absorbing material (Adachi and Buseck 2008; Zhang et al. 2008). The particles are coated by volatile species condensing onto the soot particles. The coating process typically happens rapidly, and in-situ measurements show that atmospheric soot aerosol is commonly dominated by heavily coated particles (Adachi and Buseck 2008; Adachi et al. 2010; China et al. 2013; Worringen et al. 2008). Transmission electron microscopy (TEM) images reported by Johnson et al. (2005) indicate coagulation as an additional mechanism causing internal mixing.

The condensation of coating material onto a soot aggregate causes structural changes of the aggregate as it starts to collapse. Therefore, the aggregate becomes more compact. The speed of this collapse depends on the coating material (Bambha et al. 2013; Ghazi and Olfert 2013; Pei 2018; Schnitzler et al. 2014; Zhang et al. 2008). A compaction of an aggregate can be described and quantified by an increase in its fractal dimension D_f.

Studying the effects of coating material on optical properties requires parametrisations of the coated particles. Radiative forcing calculations performed in global climate models usually rely on spherical particle models (Adachi et al. 2010; Bond et al. 2013), since these models are computationally inexpensive (see Sec. 4.3). One of the simplest parametrisations is an external mixture of volume-equivalent spheres representing pure soot and pure coating material. However, they tend to underestimate the absorption cross sections (Kahnert et al. 2012). Other rather simple model parametrisations are core shell-models, which assume a spherical black carbon core enclosed in a spherical shell. Owning to their simplicity and the low computational cost core-shell models are employed in climate models (Adachi et al. 2010; Jacobson 2001) too. A microphysical quantity, which impacts on optical cross sections, is the amount of black carbon mass interacting with electromagnetic waves (Chakrabarty and Heinson 2018). In case of core-shell model geometries much of the soot is shielded from the incident electromagnetic wave, this results in core-shell geometries underestimating absorption (Chakrabarty and Heinson 2018; Kahnert et al. 2013), although they outperform external spherical mixtures (Kahnert et al. 2012). Homogeneous, internally mixed spheres perform better, when calculating the absorption cross sections, than both externally mixed spheres and core-shell geometries (Kahnert et al. 2012). Such homogeneous model geometries were for example used by Fierce et al. (2016) in a large-scale study. Worringen et al. (2008) showed that knowledge of the mixing state of individual particles and subsequent approximations to by suitable idealised shapes can drastically reduce errors of the optical properties. For example extinction, scattering, and absorption efficiency, single scattering albedo, and asymmetry parameter of particles with soot inclusions close to the particle surface were best reproduced with a soot-shell model. The back scatter efficiency was best reproduced by homogeneous spheres. Optical properties of particles, which were characterised by soot inclusions concentrated in a disk close to the particle centre, were best reproduced by a sandwich geometry with a soot disk in the middle of a non-absorbing sphere.

Homogeneous spheres and core-shell geometries pose a risk of misrepresenting optical cross sections, as a number of studies with 3D scans of sampled soot particles (Adachi et al. 2010) and more complex models (Adachi et al. 2010; Doner et al. 2017; Dong et al. 2015; Kahnert et al. 2013; Liu et al. 2016; Wu et al. 2017) indicated. Factors contributing to these misrepresentations include effects from lacy or compact aggregate structure (Adachi et al. 2010; Wu et al. 2017), off-centre positioning of the aggregate within the coating (Adachi et al. 2010), overlapping of neighbouring monomers, and necking (Doner et al. 2017).

As discussed in Section 4.2, the linear depolarisation ratio is zero for rotationally symmetric particles. As a consequence homogeneous spheres or concentric core-shell

models are not suitable for modelling the linear depolarisation ratio. Mishchenko et al. (2016) employed a coated spheroid model to reproduce lidar field observations of the linear depolarisation ratio. Gialitaki et al. (2020) have also succesfully used homogeneous spheroids with an adjustable refractive index for reproducing lidar observations of the linear depolarisation ratio (and the extinction-to-backscatter ratio). They found that mildly aspherical spheroids could potentially improve operational remote sensing retrievals of (stratospheric) smoke. A further discussion about spheroids in general is presented in the following section.

Open cell models, i.e., fractal soot aggregates, to which coating monomers are added, display a similar shielding effect (He et al. 2015; Liou et al. 2011) as core-shell geometries. Placing each soot monomer in a spherical coating shell, while maintaining the fractal structure, including the number of monomers, results in closed cell models. Closed cell models are frequently used (He et al. 2015; Kahnert 2017; Liou et al. 2011; Liu and Mishchenko 2018; Luo et al. 2018; Mishchenko et al. 2016; Wu et al. 2014). Unlike open cell models, they do not suffer from an increased shielding of black carbon mass (He et al. 2015). This makes them suitable for calculating the absorption cross section. Most applications of closed cell models assumed the monomers and their respective coating shell to be concentrical. Luo et al. (2018) showed that introducing off-centre black carbon monomers, does not affect the optical properties. However, closed cell models do pose a risk of underestimating the linear depolarisation ratio for aggregates with a higher amount of coating material (Kahnert 2017; Liu and Mishchenko 2018).

Heavily coated soot particles are frequently parametrised as spheres with an inserted or attached aggregate. The former representing condensation and the latter coagulation. However, many of these modelling studies focused on optical cross section, asymmetry parameter and single scattering albedo (Dong et al. 2015; Liu et al. 2017; Wu et al. 2016, 2015). Wu et al. (2015) found that the optical cross sections are insensitive to whether monomers intersection with the coating sphere or not. The depolarisation by such models was investigated by Liu and Mishchenko (2018) and Mishchenko et al. (2016).

Models being capable of modelling linear depolarisation ratios for both thinly and thickly coated soot aggregates were proposed by Kahnert (2017) and Ishimoto et al. (2019). The model by Kahnert (2017) mimics film-coating by adding coating material layer by layer onto the aggregate. The coating material is restricted to lie within a sphere circumscribing the entire aggregate. The coating procedure stops, when a predefined soot volume fraction is reached. Should the circumscribing sphere be filled before the predefined soot volume fraction is reached, the coating will follow the spherical shape, hence grow radially. The coating model by Ishimoto et al. (2019) used surface potential calculations, which mimic surface-tension induced physical processes during coating the aggregate. With increasing amount of coating material the particles become gradually more spherical. Both models will result in spherical coating only for very thickly coated soot aggregates. They consequently give comparatively high values of the linear depolarisation ratio and pose the risk of overestimating it.

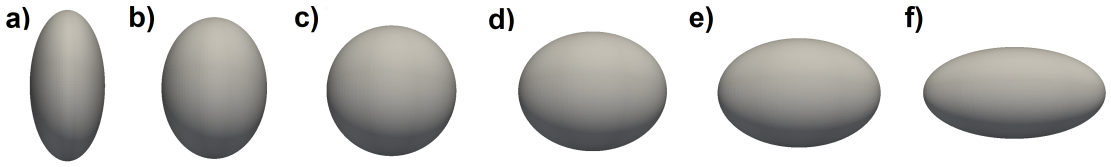

Figure 5.2: Spheroids with different aspect ratios, 0.5 (a), 0.75 (b), 1 (i.e., a sphere, c), 1.25 (d), 1.5 (e), and 2.0 (f).

5.2 Mineral dust

Mineral dust aerosol mainly originates from the Earth's arid and semi-arid regions (see Chapter 2). Images obtained by scanning electron microscopy (SEM) and by TEM indicate that mineral dust particles are usually irregular in shape, have varying degrees of surface roughness, can have complex internal structures and may consist of different minerals (e.g. Gómez Martín et al. 2021; Järvinen 2016; Jeong and Nousiainen 2014; Kemppinen et al. 2015; Lin et al. 2018; Muñoz et al. 2012, 2007; Wiegner et al. 2009). A well established model geometry, frequently employed to calculate optical properties of mineral dust aerosol are spheroids (e.g. Gasteiger et al. 2011; Mishchenko et al. 1997; Wiegner et al. 2009). Less often used is its more general form, the ellipsoid, which also can reproduce measured optical properties of dust, namely the asymmetry parameter, the single scattering albedo, and the scattering matrix elements (Merikallio et al. 2013).

In a Cartesian coordinate system with coordinate axes x, y, and z an ellipsoid can be represented by

$$\left(\frac{x}{a}\right)^2 + \left(\frac{y}{b}\right)^2 + \left(\frac{z}{c}\right)^2 = 1. \tag{5.4}$$

a, b, and c determinate the extent along the respective Cartesian axis. Under the assumption of $a = b$ the ellipsoid becomes a spheroid. The ratio a/c, the aspect ratio, with c the extent along the main rotational axis and a the maximum extent along the axis perpendicular to the main axis, then becomes a free parameter to tune the particle shape. For $a = c$ or $a/c = 1$ the resulting shape is a sphere. Aspect ratios below 1 result in prolate spheroids, whereas, spheroids are oblate, if $a/c > 1$. Fig. 5.2 shows examples of spheroids with different aspect ratio, ranging from a prolate spheroid with $a/c = 0.5$ (on the left) to an oblate spheroid with $a/c = 2$ (on the right).

Particle samples indicate that dust particles are elongated (Kandler et al. 2009; Wiegner et al. 2009). From such measurements dust particles can be fitted as spheroids with mean aspect ratios ranging from 1.3 to 1.8 (Kandler et al. 2009), highlighting the usefulness of spheroids to model optical properties of mineral dust aerosol. Spheroids are a highly versatile model, as they allow modelling a broader range of Mueller matrix elements then other geometries (Nousiainen et al. 2011, 2006). As a consequence, spheroids can also cover a large range of values of the linear depolarisation ratio. For example, the Aerosol Robotic Network (AERONET), a network of ground-based sun photometers (see Section 3.1), relies for retrievals on scattering matrix elements based on spheroidal model particles with a wide range of

size bins and aspect ratios, and several values of the refractive index (Dubovik et al. 2006).

Another type of particle models used to calculate optical properties of mineral dust are so called Gaussian random spheres. This class of model geometries was proposed by Muinonen et al. (1996) and consists of a sphere superimposed with Gaussian random perturbations. A Gaussian random sphere is characterised by a radial standard deviation σ_r, which indicates the magnitude of the perturbations and the correlation angle Γ, which describes the angular frequency of the perturbations. The smaller the value of Γ is, the larger is the perturbation frequency. Muñoz et al. (2007) and Veihelmann et al. (2006) used Gaussian random spheres to calculate Stokes matrix elements. Muñoz et al. (2007) compared the model results with measured data, and showed that spiky Gaussian random spheres resulted in better agreement than model particles visually resembling the dust sample's particles. In the resonance regime particle irregularities, represented with Gaussian random perturbations, have a strong influence on integral scattering properties, specifically extinction efficiency, symmetry parameter and single-scattering albedo (Liu et al. 2015c).

Further studies involved model particles, which possess plane surfaces, such as prisms (Bi et al. 2010; Nousiainen et al. 2006), convex polyhedra (Gasteiger et al. 2011; Torge et al. 2011), and convex fractal polyhedra (Liu et al. 2013). Torge et al. (2011) used convex polyhedra to calculate the radiative forcing. Compared to the corresponding spheroids, convex polyhedra, which are referred as edged particles by Gasteiger et al. (2011), increase both backscattering coefficient and linear depolarisation ratio. The same effect was observed for large, distorted aggregate particles. While results from polyhedral prisms can provide good agreement for the phase function and other scattering matrix elements for feldspar samples, they were found to be less versatile than spheroids. The light scattering of prisms is insensitive to changes of aspect ratios and cross-sectional shape (Nousiainen et al. 2006).

As SEM and TEM images reported by Jeong and Nousiainen (2014) and Kemppinen et al. (2015) show, mineral dust particles do not tend to have a homogeneous mineralogical composition, but have different internal structures and mineralogy. Especially hematite inclusions have particularly strong impacts on optical properties, such as the scattering matrix elements, asymmetry parameter, extinction-to-backscatter ratio, and linear depolarisation ratio. These effects can be even more pronounced in the presence of pores. Such internal structures appear to have a stronger impact on scattering matrix elements, than small surface roughness (Kemppinen et al. 2015). While for the comparatively realistic shapes used by Kemppinen et al. (2015) inhomogeneities in form of inclusions and coatings reduced the linear depolarisation ratio, inclusions were found to induce linear depolarisation ratios of up to 0.6 in spherical shapes (Kahnert 2015). As a consequence, inhomogeneities, especially those with a strong contrast in refractive index are a potentially important morphological feature of mineral dust (Kahnert 2015; Kemppinen et al. 2015).

5.3 Sea salt

Compared to the previous two aerosol types, soot and mineral dust, only very few investigations have considered morphologically realistic particle models in aerosol optics simulations. Similarly to (coated) soot and mineral dust extinction and absorption cross sections were modelled by spherical particles (Adachi and Buseck 2015; Chamaillard et al. 2006).

Images from sampled dry sea salt particles (Gwaze et al. 2007; Haarig et al. 2017; McInnes et al. 1994; Wise et al. 2005; Zeng et al. 2013) indicate a cube-like particle shapes. As a consequence, cubical (Adachi and Buseck 2015; Chamaillard et al. 2006; David et al. 2013; Sakai et al. 2010) and cuboidal particle models (Adachi and Buseck 2015) have also been used for modelling optical cross sections or efficiencies. Non-spherical shapes generally enhance the total scattering coefficients and hemispheric backscattering coefficients[1](Chamaillard et al. 2006). Light scattering by flat and elongated cuboids can differ to up to 200% from results from spherical model particles. Cubes were also used for studying linear depolarisation ratio (Haarig et al. 2017; Murayama et al. 1999). They can be considered as a canonical reference shape for sea salt aerosol.

Bi et al. (2018b) proposed the use of superellipsoids for modelling optical properties of sea salt aerosol. Superellipsoids in a Cartesian coordinate system can mathematically described by (Bi et al. 2018b; Wriedt 2002)

$$\left[\left(\frac{x}{a}\right)^{\frac{2}{e}} + \left(\frac{y}{b}\right)^{\frac{2}{e}}\right]^{\frac{e}{n}} + \left(\frac{z}{c}\right)^{\frac{2}{n}} = 1 \tag{5.5}$$

As in Eq. 5.4 a, b, and c define the particle's extend along the x-, y, amd z-axis, respectively. n and e denote the roundness parameters in north-south (or polar) and east-west (or azimuthal) directions. By changing n and e the overall particle shape is affected, allowing to obtain cubes, spheres, cylinders, or octahedra (Barr 1981; Bi et al. 2018a; Wriedt 2002). This led to superellipsoids being used in computer graphics (Barr 1981). Examples of superellipsoidal geometries with equal aspect ratios ($a = b = c$) and equal roundness parameters ($n = e$) are shown in Fig. 5.3, strictly speaking the resulting shapes are superspheres. From left to right Fig. 5.3 show superellipsoids with a) $n = e = 0.0$ (a cube), b) $n = e = 0.5$ (a rounded cube), c) $n = e = 1.0$ (a sphere), d) $n = e = 1.5$ (a rounded octahedron), e) $n = e = 2.0$ (a octahedron), and f) $n = e = 2.5$ (a concave octahedron).

Bi et al. (2018b) used both homogeneous, representing pure sea salt, and inhomogeneous superellipsoids, representing water-coated sea salt particles, and spheres with superellipsoidal inclusions to calculate the linear depolarisation ratio. The range of possible shapes was limited by assuming $a = b$, and $n = e$, resulting in superspheroids. The superspheroids are capable of reproducing laboratory measurements of the linear depolarisation ratio in near-backscattering direction.

[1]These quantities are defined analogously to the backscattering coefficient β as given in Eq. 4.18.

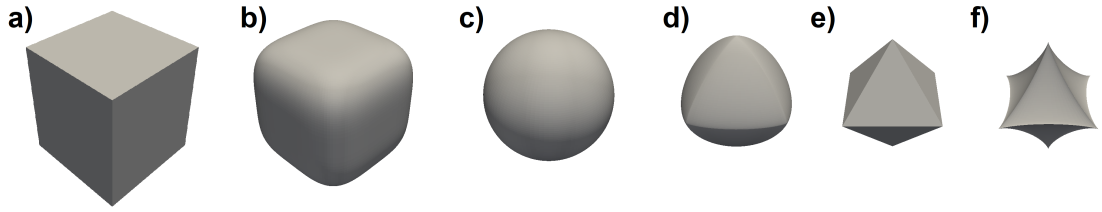

Figure 5.3: Examples of superellipsoids, with aspect ratios of 1 ($a = b = c$), and equal roundness parameters ($n = e$). The roundness parameters increase from left to right with a) $n = 0.0$ (i.e., a cube), b) $n = 0.5$, c) $n = 1.0$ (i.e., a sphere), d) $n = 1.5$, e) $n = 2.0$ (i.e., an octahedron), and f) $n = 2.5$

5.4 Using particle models in Bayesian retrievals

Finding an atmospheric state x based on observations y represents an ill-posed inverse problem. Ill-posed inverse problems were already briefly introduced in Sec. 3.3. To be more specific, one tries to find the conditional probability that the atmosphere is in state x, given the observations y, expressed by $P(x|y)$. $P(x|y)$ can be determined using Bayes' theorem (Rodgers 2000)

$$P(x|y) = \frac{P(y|x)P(x)}{P(y)}. \tag{5.6}$$

$P(x|y)$ is the posterior probability density function of the state, when the measurement is given. $P(x)$ is the prior knowledge, which is in remote sensing and inverse modelling referred to as a priori and in data assimilation as background (Kahnert and Andersson 2017). The knowledge of y that would be obtained if the state were x is described by $P(y|x)$ and also called the observation's likelihood. $P(y)$ is practically a normalising factor, which is formally obtained by integrating $P(y|x)P(x)$ over all x (Rodgers 2000). By assuming that the probability density functions follow a Gaussian distribution, $P(x)$ and $P(y|x)$ can be expressed as (Bouttier and Courtier 1999; Kalnay 2003):

$$P(x) = \frac{1}{(2\pi)^{n/2}|B|^{1/2}} \exp\left(-\frac{1}{2}(x - x_b)^T B^{-1}(x - x_b)\right), \tag{5.7}$$

$$P(y|x) = \frac{1}{(2\pi)^{p/2}|R|^{1/2}} \exp\left(-\frac{1}{2}(y - H(x))^T R^{-1}(y - H(x))\right). \tag{5.8}$$

The background, x_b, is a previous estimate of the model state, usually obtained by climatology or a previous forecast. B and R denote error covariance matrices with dimension n and p respectively. The determinant of the respective matrix is indicated by $|\cdot|$. The observation operator H transforms model variables to observation space. The observation errors are often uncorrelated. Even if the errors are correlated, the correlations are often neglected. In this case, the error covariance matrix R becomes diagonal, and the diagonal elements contain the observation error variances[2].

[2]The error covariance matrix R, discussed in this section and the backscatter ratio $\mathbf{R}$ discussed in Section 3.2 share the same symbol, but they are not related.

There are several contributors to the observations error, such as the measurement error, forward model errors, representative errors (in case of operational models). The forward model error depends on the uncertainties in the aerosol optics model. Accurate aerosol optics models and accurate uncertainty estimates are a prerequisite for maximising the extraction of information from optical measurements, while also avoiding the extraction of noise. A possible way to estimate the contribution of the forward model's uncertainties to the observation error variances is to compare properties from simplified models to more complex models or measurements (Kahnert and Andersson 2017). Obtaining $P(y|x)$ and by extension $P(x|y)$ requires that the uncertainties in the forward model only introduce random errors, but not any biases in the inversion method.

Chapter 6

Summary of Appended Articles

6.1 Paper A: Calculation of optical properties of light-absorbing carbon with weakly absorbing coating: A model with tunable transition from film-coating to spherical-shell coating

Based on a previous study by Kahnert (2017) a coated aggregate model with a tunable transition between film coating and spherical shell coating is presented. Coating material is added layer by layer in small volume elements onto an aggregate. The coating material is further restricted to lie within an imaginary sphere with variable diameter D_c. The diameter of this sphere is obtained by taking each aggregate's largest dimension D and multiply it with a constant factor f_c, hence $D_c = f_c D$. The tunable size of this sphere parametrizes different transition speed between film-coating, i.e. coating material following the aggregate shape, and spherical shell coating, i.e. radial growth. A smaller diameter of this imaginary sphere would correspond to a more rapid transition to spherical growth. In contrast to the earlier study by Kahnert (2017) it was also assumed that with increasing coating thickness the compactness of the soot aggregate increases by increasing the fractal dimesion D_f.

Two different values for the critical diameter were tested, $f_c = 0.6$, representing a rapid transition between film-coating and radial growth and $f_c = 1.0$, i.e., a slow transition. As hypothesised, the model particles with $D_c = 0.6 \cdot D$ result in lower values of the linear depolarisation ratio, which are consistent with reported values from lidar field observations. The model with $D_c = 1.0 \cdot D$, poses the risk of overestimating the linear depolarisation ratio, when compared to lidar field observations. The uncertainty in optical propeties pertaining to various sources of uncertainty in microphysical properties (aggregate structure, as reflected by changes in fractal dimension, fractal prefactor, and monomer radius and chemical composition, as reflected by changes in coating and soot refractive index) was estimated. All calculations were performed at $\lambda = 355\,\text{nm}$ and 532 nm.

Contributions: Implementing the tunable transition, performing the calculations and

writing the article's first draft, contributing to article editing.

6.2 Paper B: Coating material-dependent differences in modelled lidar-measurable quantities for heavily coated soot particles

Uncertainty estimates in Paper A showed that for thickly coated soot aggregates the chemical composition of coating material as reflected by the refractive index is one of the largest sources of uncertainty. This study investigates, if the coating material-induced differences in linear depolarisation ratio in backscattering direction, extinction-to-backscatter ratio, and Ångström exponents may be considered as an additional source of information. To this end optical properties of heavily coated soot (with a soot volume fraction of $f_{\mathrm{vol}} = 0.07$) were calculated for two different coating materials (an inorganic material, sulphate, and an organic, toluene-based material) at three different wavelengths (355 nm, 532 nm, and 1064 nm). To obtain size-averaged optical properties different particle sizes were considered. The aggregate size was controlled by the number of monomers, which ranged from 26 to 1508 in 58 linearly equidistant steps. Per size five different stochastical realisations were considered. The depolarisation ratio, the extinction-to-backscatter ratio and the lidar-relevant Ångström exponents were size-averaged assuming different log-normal size distributions based on reported in-situ measurements.

With exception of the extinction Ångström exponent between 355 and 532 nm and the linear depolarisation ratio at 1064 nm the size-averaged optical properties were distinct. As a consequence, it is potentially possible to distinguish between inorganic coating material and toluene-based, organic coating material with the help of lidar measurements. Rather than being a source of uncertainty the coating material's refractive index may be considered as a source of information.
Contributions: Contributing to study design, performing the calculations and writing the article's first draft, contributing to article editing.

6.3 Paper C: Aerosol optics model for black carbon applicable to remote sensing, chemical data assimilation, and climate modelling

A review study, not included in this thesis (Kahnert and Kanngießer 2020), identified the soot mass interacting with the incident electromagnetic wave as a key parameter affecting the absorption of a (coated) soot particle. The linear depolarisation ratio of an individual coated soot particle was found to depend mainly on the particle's non-sphericity. Paper C aimed at combining these two insights to create a single, simplified particle model, which simultaneously allows to tune the model with respect to absorption and depolarisation of soot particles. The model proposed in Paper A was employed as a reference model of coated soot aggregates.

A model of aggregates partially embedded in a spherical shell, so that the individual spheres are always in point-contact, as originally introduced by Wu et al. (2015), was tested. The number of monomers within the spherical coating shell is a free parameter to tune the model. The larger the number of monomers inside the coating with a fixed number of total monomers is, the more spherical the overall particle shape becomes. It was hypothesis that the linear depolarisation ratio decreases accordingly. This first model has two main drawbacks. Its relative complexity could still limit large-scale applications, although it is considerable less complex than the reference model. Second, the spherical coating results in an underestimation of linear depolarisation ratios, as only a range between roughly 0.03 and 0.09 is covered, while field observations indicate size-averaged values of up to 0.23.

A second model tested is the core-grey shell dimer (CGS2), which extends previous core-grey shell (CGS) geometries. This model mixes an adjustable fraction of the soot core homogeneously with the coating material, which increases the soot mass interacting with the electromagnetic wave. Due to its concentrical and spherical shape the CGS model is unsuitable for determining the linear depolarisation value. Non-sphericity is introduced by dividing the total particle mass into two core-grey shell particles, which then are combined into a dimer. The absorption cross section depends mainly on the amount of soot in the core, and the depolarisation ratio can be tuned by changing the relative size of the two spheres in the dimer. Linear depolarisation ratio, extinction, backscattering and absorption cross section of the reference model can be fitted reasonably well using the CGS2 model. Calculations were performed at a wavelength of $\lambda = 0.532\,\mu$m.
Contributions: Contributing to writing and editing, performing part of the calculations

6.4 Paper D: Aerosol-optics model for the backscatter depolarisation ratio of mineral dust particles

For 131 samples of mineral dust with different size distributions, morphology, and composition the linear backscattering depolarisation ratio in near-backscattering direction ($\vartheta = 178°$) was measured in the AIDA (Aerosol Interaction and Dynamics in the Atmosphere) chamber at a wavelength of $\lambda = 488\,$nm. Spheroidal model particles with widely ranging aspect ratios and refractive indices were employed to find a minimum-bias and minimum-variance fit. The best fit was achieved for prolate spheroids with an aspect ratio of $a/b = 0.87$ and a complex refractive index of $m = 1.525 + i0.001$. Uncertainty estimates were performed for changes in refractive index, inhomogeneity, surface roughness, size-distribution shape, and aspect ratio. The measurement values' variation was found to be explained best by a combination of surface roughness, refractive index, and, although to a lesser extend, geometric variance of the log-normal size distribution. Changes in aspect ratio by far exceed the range of observations. There is certain flexibility in using aspect-ratio distributions to reproduce the observations with shapes confined to mildly aspherical shapes.

Contributions: Contributing to study design, performing part of the calculations and contributing to writing the article.

6.5 Paper E: Modeling optical properties of non-cubical sea salt particles

Paper E focuses on dry sea salt aerosol. The capabilities of superellipsoids to simultaneously model the linear backscatter depolarisation ratio and the extinction-to-backscatter ratio are tested. To quantify potential uncertainties stemming mainly from non-ideal shapes compared to simplified shapes Gaussian random cubes and convex (irregular) polyhedra are used. All calculations were performed at a wavelength of $\lambda = 0.532\,\mu$m. To gauge the range of values five stochastic realisation per model instance of the convex polyhedra and of the Gaussian random cubes were used. Uncertainties in both the real and the imaginary part of the refractive index. Size-averaged superellipsoids with effective radii between 1.0 and 1.6 μm can simultaneously produce values of the linear backscatter depolarisation ratio and the extinction-to-backscatter ratio consistent with values reported from lidar field measurements. The effective radii cover a range, which is typical for marine aerosol at low to moderate wind speeds. Convex polyhedra are generated by randomly placing N_c points in a Cartesian coordinate system, around which a convex hull is constructed using standard algorithms. The value of N_c impacts the shape. The optical properties of convex polyhedra generally scatter around the reference values obtained from cubes. For $N_c = 10$ the shapes differ substantially from cubes,i.e., they introduce a bias compared to cubes. For $N_c = 1000$ the shapes are rather similar to cubes. Thus, the variation in the optical properties is small. Convex polyhedra with $N_c \sim 100$ provide a promising approach for future studies. By contrast Gaussian random surface perturbations introduce a bias in the optical properties when compared to the cubical reference shape. The linear depolarisation ratio is increased the stronger the resulting shape deviates from a cube, i.e. the larger the radial standard deviation and the smaller the correlation angle are. Compared to Paper D, in which Gaussian random perturbations of spheroids are found a suitable way of estimating uncertainties, this is an entirely unexpected finding. The refractive index was found to be a potential important tuning parameter as well as an essential source of uncertainty.
Contributions: Contributing to study design, performing DDA calculations and writing the article's first draft, contributing to editing.

6.6 Paper F: Optical properties of water-coated sea salt model particles

This study investigates water-coated sea salt aerosol. A coated convex polyhedra model is proposed, which is based on the convex polyhedra model from Paper E. Using surface potential calculations a water coating is added and the salt crystal is

partially dissolved by transforming salt volume elements to coating elements. Using the coated convex polyhedra model the optical cross sections, the extinction-to-backscatter ratio, and the linear depolarisation ratio in backscattering direction are calculated at a wavelength of $\lambda = 0.532\,\mu$m. A non-concentrical spherical shell model was then used to investigate off-centre inhomogeneities as a potential refinement of the coated convex polyhedra model. Off-centre inhomogeneities in the non-concentric spherical shell model have a considerable impact on the optical properties. The actual necessity of incorporating off-centre inhomogeneities into the coated convex polyhedra model needs to be determined with future laboratory measurements. The convex polyhedra model is further used as a reference model and is fitted with three simplified models, homogeneous superellipsoids, inhomogeneous superellipsoids, and cube-sphere hybrids. The three simplified models were found to perform similarly and can reproduce the optical properties of the reference model. The homogeneous model particles can compensate for inhomogeneity effects by increasing the non-sphericity. *Contributions:* performing DDA, MSTM calculations, study design, writing first draft, contributing to editing

Chapter 7

Conclusion and Outlook

This thesis aims to contribute to a better understanding of the links between aerosol microphysical properties, specifically morphology and composition, and the corresponding optical properties. A strong focus is placed on (but the work is not limited to) the linear depolarisation ratio in (near-)backscattering direction. To this end advances have been made, as can be seen in the appended papers. For coated soot aerosol and for dry and partially dissolved sea salt aerosol new morphologically complex particle models have been proposed. For coated soot, mineral dust, and (partially dissolved) sea salt aerosol simplified model particles have been proposed, which capture essential features, such as the soot core fraction and the non-sphericity.

The simplified models can be employed in applications requiring large-scale calculations. From a combination of such simplified models with more complex models uncertainties can be inferred. An example for such a combination is given in Paper D.

Based on the research presented in this thesis, there are several avenues for future studies. The morphologically complex aerosol particle models proposed in Papers A, E, and F, namely for coated soot and dry and partially dissolved sea salt, require further validation using laboratory studies of both particle morphology and the particles' optical properties. Paper F also proposes potential refinements, for which the necessity needs to be gauged in laboratory experiments. So far, it has been demonstrated that they produce results consistent with reported lidar field measurements.

Future studies should also extend the wavelengths at which the models, especially the models presented in Papers C-F, are employed, to at least $\lambda = 355\,\mathrm{nm}$ and $\lambda = 1064\,\mathrm{nm}$. This would allow investigating the models' capabilities to reproduce spectral behaviour and could guide further attempts to refine the proposed models.

Paper B showed that for a fixed coating thickness two different coating materials result in distinct optical properties. However, in atmospheric samples a certain degree of variation with respect to the coating thickness is expected. Effects of a coating mass distribution on the optical properties and, thus, on the potential of differentiating coating materials, are yet to be investigated. One conclusion of Paper B was that optical materials can potentially be distinguished based on their optical

properties. With the help of synthetic lidar measurements this could be further tested.

The coated convex polyhedra model for partially dissolved sea salt aerosol, proposed in Paper F is currently used for studying lidar measurements of sea salt aerosol. This includes also calculations over a large size range at the wavelengths of $\lambda = 355\,\mathrm{nm}$ and $\lambda = 1064\,\mathrm{nm}$.

Mineral dust and sea salt aerosol particles are the two most abundant aerosol particle types in the atmosphere. Black carbon aerosol, although less abundant, has a considerable impact on the Earth's climate. Volcanic ash, which is less abundant than mineral dust and sea salt aerosol and has a lower impact on the Earth's climate than black carbon, has not been studied in this thesis. However, its potentially strong impacts on aviation may warrant future studies of its polarimetric properties.

Since aerosol types, especially after a prolonged residence time in the atmosphere, tend to mix, the proposed particle models could aid in disentangling such particle mixtures with the help of information content analysis. Such an analysis would be among the next steps towards the long term goal of assimilating lidar measurements into chemical transport models, to which this thesis contributes.

Bibliography

Adachi, K. and P. R. Buseck (2008). "Internally mixed soot, sulfates, and organic matter in aerosol particles from Mexico City". *Atmos. Chem. Phys.* 8.21, pp. 6469–6481. DOI: 10.5194/acp-8-6469-2008 (cit. on p. 31).

Adachi, K. and P. R. Buseck (2015). "Changes in shape and composition of sea-salt particles upon aging in an urban atmosphere". *Atmos. Environ.* 100, pp. 1–9. DOI: 10.1016/j.atmosenv.2014.10.036 (cit. on p. 36).

Adachi, K., S. H. Chung, and P. R. Buseck (2010). "Shapes of soot aerosol particles and implications for their effects on climate". *J. Geophys. Res.* 115.D15, n/a–n/a. DOI: 10.1029/2009JD012868 (cit. on pp. 31, 32).

Anenberg, S. C., K. Talgo, S. Arunachalam, P. Dolwick, C. Jang, and J. J. West (2011). "Impacts of global, regional, and sectoral black carbon emission reductions on surface air quality and human mortality". *Atmos. Chem. Phys.* 11.14, pp. 7253–7267. DOI: 10.5194/acp-11-7253-2011 (cit. on p. 10).

Anenberg, S. C., J. Schwartz, D. Shindell, M. Amann, G. Faluvegi, Z. Klimont, G. Janssens-Maenhout, L. Pozzoli, R. Van Dingenen, E. Vignati, L. Emberson, N. Z. Muller, J. J. West, M. Williams, V. Demkine, W. K. Hicks, J. Kuylenstierna, F. Raes, and V. Ramanathan (2012). "Global Air Quality and Health Co-benefits of Mitigating Near-Term Climate Change through Methane and Black Carbon Emission Controls". *Environ. Health Perspect.* 120.6. DOI: 10.1289/ehp.1104301 (cit. on p. 10).

Ansmann, A. and D. Müller (2005). "Lidar and Atmospheric Aerosol Particles". In: *Lidar*. Ed. by C. Weitkamp. Vol. 102. Springer Series in Optical Sciences. Springer, New York, NY, pp. 105–141. DOI: 10.1007/0-387-25101-4_4 (cit. on pp. 13, 15–17).

Ansmann, A., F. Wagner, D. Müller, D. Althausen, A. Herber, W. von Hoyningen-Huene, and U. Wandinger (2002). "European pollution outbreaks during ACE 2: Optical particle properties inferred from multiwavelength lidar and star-Sun photometry". *J. Geophys. Res.* 107.D15, AAC 8-1–AAC 8-14. DOI: 10.1029/2001JD001109 (cit. on p. 25).

Bambha, R. P., M. A. Dansson, P. E. Schrader, and H. A. Michelsen (2013). "Effects of volatile coatings and coating removal mechanisms on the morphology of graphitic soot". *Carbon* 61, pp. 80–96. ISSN: 0008-6223. DOI: 10.1016/j.carbon.2013.04.070 (cit. on p. 32).

Barr, A. H. (1981). "Superquadrics and Angle-Preserving Transformations". *IEEE Comput. Graphics Appl.* 1.1, pp. 11–23. ISSN: 1558-1756. DOI: 10.1109/MCG.1981.1673799 (cit. on p. 36).

Bi, L., W. Lin, D. Liu, and K. Zhang (2018a). "Assessing the depolarization capabilities of nonspherical particles in a super-ellipsoidal shape space". *Opt. Express* 26.2, pp. 1726–1742. DOI: 10.1364/OE.26.001726 (cit. on pp. 25, 36).

Bi, L., W. Lin, Z. Wang, X. Tang, X. Zhang, and B. Yi (2018b). "Optical Modeling of Sea Salt Aerosols: The Effects of Nonsphericity and Inhomogeneity". *J. Geophys. Res.* 123.1, pp. 543–558. DOI: 10.1002/2017JD027869 (cit. on p. 36).

Bi, L., P. Yang, G. W. Kattawar, and R. Kahn (2010). "Modeling optical properties of mineral aerosol particles by using nonsymmetric hexahedra". *Appl. Opt.* 49.3, pp. 334–342. DOI: 10.1364/AO.49.000334 (cit. on p. 35).

Böckmann, C. (2001). "Hybrid regularization method for the ill-posed inversion of multiwavelength lidar data in the retrieval of aerosol size distributions". *Appl. Opt.* 40.9, pp. 1329–1342. DOI: 10.1364/AO.40.001329 (cit. on p. 15).

Bohren, C. F. and D. R. Huffman (1983). *Absorption and scattering of light by small particles*. Wiley New York. ISBN: 978-0-471-29340-8 (cit. on pp. 23, 24, 26).

Bond, T. C., S. J. Doherty, D. W. Fahey, P. M. Forster, T. Berntsen, B. J. DeAngelo, M. G. Flanner, S. Ghan, B. Kärcher, D. Koch, S. Kinne, Y. Kondo, P. K. Quinn, M. C. Sarofim, M. G. Schultz, M. Schulz, C. Venkataraman, H. Zhang, S. Zhang, N. Bellouin, S. K. Guttikunda, P. K. Hopke, M. Z. Jacobson, J. W. Kaiser, Z. Klimont, U. Lohmann, J. P. Schwarz, D. Shindell, T. Storelvmo, S. G. Warren, and C. S. Zender (2013). "Bounding the role of black carbon in the climate system: A scientific assessment". *J. Geophys. Res.* 118.11, pp. 5380–5552. DOI: 10.1002/jgrd.50171 (cit. on pp. 9, 10, 29, 32).

Bond, T. C. and R. W. Bergstrom (2006). "Light Absorption by Carbonaceous Particles: An Investigative Review". *Aerosol Sci. Technol.* 40.1, pp. 27–67. DOI: 10.1080/02786820500421521 (cit. on pp. 9, 30).

Boucher, O. (2015). *Atmospheric Aerosols - Properties and Climate Impacts*. Springer, Dordrecht. ISBN: 978-94-017-9649-1. DOI: 10.1007/978-94-017-9649-1 (cit. on pp. 7–9, 11, 12).

Bouttier, F. and P. Courtier (1999). *Data assimilation concepts and methods*. ECMWF Meteorological Training Course Lecture Series (cit. on p. 37).

Brasil, A., T. Farias, and M. Carvalho (1999). "A RECIPE FOR IMAGE CHARACTERIZATION OF FRACTAL-LIKE AGGREGATES". *J. Aerosol Sci.* 30.10, pp. 1379–1389. DOI: 10.1016/S0021-8502(99)00026-9 (cit. on p. 31).

Bristow, C. S., K. A. Hudson-Edwards, and A. Chappell (2010). "Fertilizing the Amazon and equatorial Atlantic with West African dust". *Geophysical Research Letters* 37.14. DOI: https://doi.org/10.1029/2010GL043486 (cit. on p. 10).

Buseck, P. R. and M. Pósfai (1999). "Airborne Minerals and Related Aerosol Particles: Effects on Climate and the Environment". *Proceedings of the National Academy of Sciences of the United States of America* 96.7, pp. 3372–3379. ISSN: 00278424 (cit. on pp. 9, 10).

Carrillo, J., J. C. Guerra, E. Cuevas, and J. Barrancos (2016). "Characterization of the Marine Boundary Layer and the Trade-Wind Inversion over the Sub-tropical North Atlantic". *Boundary Layer Meteorol.* 158.2, pp. 311–330. ISSN: 1573-1472. DOI: 10.1007/s10546-015-0081-1 (cit. on p. 7).

Casadevall, T. J. (1994). "The 1989–1990 eruption of Redoubt Volcano, Alaska: impacts on aircraft operations". *J. Volcanol. Geotherm. Res.* 62.1. The 1989-1990 Eruptions of Redoubt Volcano, Alaska, pp. 301–316. ISSN: 0377-0273. DOI: 10.1016/0377-0273(94)90038-8 (cit. on p. 10).

Ceolato, R., L. Paulien, J. B. Maughan, C. M. Sorensen, and M. J. Berg (2020). "Radiative properties of soot fractal superaggregates including backscattering and depolarization". *J. Quant. Spectrosc. Radiat. Transfer*, p. 106940. ISSN: 0022-4073. DOI: https://doi.org/10.1016/j.jqsrt.2020.106940 (cit. on pp. 21, 23, 31).

Chakrabarty, R. K. and W. R. Heinson (2018). "Scaling Laws for Light Absorption Enhancement Due to Nonrefractory Coating of Atmospheric Black Carbon Aerosol". *Phys. Rev. Lett.* 121 (21), p. 218701. DOI: 10.1103/PhysRevLett.121.218701 (cit. on p. 32).

Chamaillard, K., C. Kleefeld, S. Jennings, D. Ceburnis, and C. O'Dowd (2006). "Light scattering properties of sea-salt aerosol particles inferred from modeling studies and ground-based measurements". *J. Quant. Spectrosc. Radiat. Transfer* 101.3. Light in Planetary Atmospheres and Other Particulate Media, pp. 498–511. ISSN: 0022-4073. DOI: https://doi.org/10.1016/j.jqsrt.2006.02.062 (cit. on p. 36).

China, S., C. Mazzoleni, K. Gorkowski, A. C. Aiken, and M. K. Dubey (2013). "Morphology and mixing state of individual freshly emitted wildfire carbonaceous particles". *Nat. Commun.* 4.2122. DOI: 10.1038/ncomms3122 (cit. on p. 31).

David, G., B. Thomas, T. Nousiainen, A. Miffre, and P. Rairoux (2013). "Retrieving simulated volcanic, desert dust and sea-salt particle properties from two/three-component particle mixtures using UV-VIS polarization lidar and T matrix". *Atmos. Chem. Phys.* 13, pp. 6757–6776. DOI: 10.5194/acp-13-6757-2013 (cit. on p. 36).

Davies, A. and Knyazikhin (2010). "3D Radiative Transfer in Cloudy Atmospheres". In: ed. by A. Marshak and A. Davis. Springer Berlin Heidelberg. Chap. A Primer in 3D Radiative Transfer. ISBN: 978-3-642-06303-9 (cit. on p. 24).

Doner, N. and F. Liu (2017). "Impact of morphology on the radiative properties of fractal soot aggregates". *J. Quant. Spectrosc. Radiat. Transfer* 187.Supplement C, pp. 10–19. ISSN: 0022-4073. DOI: 10.1016/j.jqsrt.2016.09.005 (cit. on p. 31).

Doner, N., F. Liu, and J. Yon (2017). "Impact of necking and overlapping on radiative properties of coated soot aggregates". *Aerosol Sci. Technol.* 51.4, pp. 532–542. DOI: 10.1080/02786826.2016.1275513 (cit. on pp. 31, 32).

Dong, J., J. Zhao, and L. Liu (2015). "Morphological effects on the radiative properties of soot aerosols in different internally mixing states with sulfate". *J. Quant. Spectrosc. Radiat. Transfer* 165.Supplement C, pp. 43–55. DOI: 10.1016/j.jqsrt.2015.06.025 (cit. on pp. 32, 33).

Draine, B. T. and P. J. Flatau (1994). "Discrete-Dipole Approximation For Scattering Calculations". *J. Opt. Soc. Am. A* 11.4, pp. 1491–1499. DOI: 10.1364/JOSAA.11.001491 (cit. on p. 26).

Dubovik, O., A. Sinyuk, T. Lapyonok, B. N. Holben, M. Mishchenko, P. Yang, T. F. Eck, H. Volten, O. Muñoz, B. Veihelmann, W. J. van der Zande, J.-F. Leon, M. Sorokin, and I. Slutsker (2006). "Application of spheroid models to account

for aerosol particle nonsphericity in remote sensing of desert dust". *J. Geophys. Res.* 111.D11, n/a–n/a. DOI: 10.1029/2005JD006619 (cit. on p. 35).

Eggersdorfer, M. L. and S. Pratsinis (2012). "The Structure of Agglomerates Consisting of Polydisperse Particles". *Aerosol Sci. Technol.* 46.3, pp. 347–353. DOI: 10.1080/02786826.2011.631956 (cit. on pp. 30, 31).

Eloranta, E. E. (2005). "High Spectral Resolution Lidar". In: *Lidar: Range-Resolved Optical Remote Sensing of the Atmosphere*. Ed. by C. Weitkamp. New York, NY: Springer New York, pp. 143–163. ISBN: 978-0-387-25101-1. DOI: 10.1007/0-387-25101-4_5 (cit. on p. 17).

Emde, C., R. Buras-Schnell, A. Kylling, B. Mayer, J. Gasteiger, U. Hamann, J. Kylling, B. Richter, C. Pause, T. Dowling, and L. Bugliaro (2016). "The libRadtran software package for radiative transfer calculations (version 2.0.1)". *Geosci. Model Dev.* 9.5, pp. 1647–1672. DOI: 10.5194/gmd-9-1647-2016 (cit. on p. 20).

Evan, A. T., J. Dunion, J. A. Foley, A. K. Heidinger, and C. S. Velden (2006). "New evidence for a relationship between Atlantic tropical cyclone activity and African dust outbreaks". *Geophys. Res. Lett.* 33.19. DOI: https://doi.org/10.1029/2006GL026408 (cit. on p. 10).

Fierce, L., T. C. Bond, S. E. Bauer, F. Mena, and N. Riemer (2016). "Black carbon absorption at the global scale is affected by particle-scale diversity in composition". *Nat. Commun.* 7.1, p. 12361. ISSN: 2041-1723. DOI: 10.1038/ncomms12361 (cit. on p. 32).

Fleisch, D. (2019). *A Student's Guide to Maxwell's Equations*. 20th ed. Cambridge University Press. 146 pp. ISBN: 978-0-521-70147-1 (cit. on p. 21).

Forster, P., T. Storelvmo, K. Armour, W. Collins, J. L. Dufresne, D. Frame, D. J. Lunt, T. Mauritsen, M. D. Palmer, M. Watanabe, M. Wild, and H. Zhang (2021). "The Earth's Energy Budget, Climate Feedbacks, and Climate Sensitivity". In: ed. by V. Masson-Delmotte, P. Zhai, A. Pirani, S. L. Connors, C. Péan, S. Berger, N. Caud, Y. Chen, L. Goldfarb, M. I. Gomis, M. Huang, K. Leitzell, E. Lonnoy, J. B. R. Matthews, T. K. Maycock, T. Waterfield, O. Yelekçi, R. Yu, and B. Zhou. Cambridge University Press. Chap. 7 (cit. on pp. 3, 9).

Fowler, D., P. Brimblecombe, J. Burrows, M. R. Heal, P. Grennfelt, D. S. Stevenson, A. Jowett, E. Nemitz, M. Coyle, X. Lui, Y. Chang, G. W. Fuller, M. A. Sutton, Z. Klimont, M. H. Unsworth, and M. Vieno (2020). "A chronology of global air quality". *Philosophical Transactions of the Royal Society A: Mathematical, Physical and Engineering Sciences* 378.2183, p. 20190314. DOI: 10.1098/rsta.2019.0314 (cit. on p. 3).

Freudenthaler, V., M. Esselborn, M. Wiegner, B. Heese, M. Tesche, A. Ansmann, D. Müller, D. Althausen, M. Wirth, A. Fix, G. Ehret, P. Knippertz, C. Toledano, J. Gasteiger, M. Garhammer, and M. Seefeldner (2009). "Depolarization ratio profiling at several wavelengths in pure Saharan dust during SAMUM 2006". *Tellus B* 61.1, pp. 165–179. ISSN: 1600-0889. DOI: 10.1111/j.1600-0889.2008.00396.x (cit. on pp. 14, 15).

Gaskins, A. J., L. Mínguez-Alarcón, K. C. Fong, S. Abdelmessih, B. A. Coull, J. E. Chavarro, J. Schwartz, I. Kloog, I. Souter, R. Hauser, and F. Laden (2019).

"Exposure to Fine Particulate Matter and Ovarian Reserve Among Women from a Fertility Clinic". *Epidemiology* 30.4. ISSN: 1044-3983 (cit. on p. 10).

Gasteiger, J., C. Emde, B. Mayer, R. Buras, S. Buehler, and O. Lemke (2014). "Representative wavelengths absorption parameterization applied to satellite channels and spectral bands". *J. Quant. Spectrosc. Radiat. Transfer* 148, pp. 99–115. ISSN: 0022-4073. DOI: 10.1016/j.jqsrt.2014.06.024 (cit. on p. 20).

Gasteiger, J., M. Wiegner, S. Groß, V. Freudenthaler, C. Toledano, M. Tesche, and K. Kandler (2011). "Modelling lidar-relevant optical properties of complex mineral dust aerosols". *Tellus B* 63.4, pp. 725–741. DOI: 10.1111/j.1600-0889.2011.00559.x (cit. on pp. 24, 34, 35).

Ghazi, R. and J. S. Olfert (2013). "Coating Mass Dependence of Soot Aggregate Restructuring due to Coatings of Oleic Acid and Dioctyl Sebacate". *Aerosol Sci. Technol.* 47.2, pp. 192–200. DOI: 10.1080/02786826.2012.741273 (cit. on p. 32).

Gialitaki, A., A. Tsekeri, V. Amiridis, R. Ceolato, L. Paulien, A. Kampouri, A. Gkikas, S. Solomos, E. Marinou, M. Haarig, H. Baars, A. Ansmann, T. Lapyonok, A. Lopatin, O. Dubovik, S. Groß, M. Wirth, M. Tsichla, I. Tsikoudi, and D. Balis (2020). "Is the near-spherical shape the "new black" for smoke?" *Atmos. Chem. Phys.* 20.22, pp. 14005–14021. DOI: 10.5194/acp-20-14005-2020 (cit. on p. 33).

Gómez Martín, J. C., D. Guirado, E. Frattin, M. Bermudez-Edo, P. Cariñanos Gonzalez, F. J. Olmo Reyes, T. Nousiainen, P. J. Gutiérrez, F. Moreno, and O. Muñoz (2021). "On the application of scattering matrix measurements to detection and identification of major types of airborne aerosol particles: Volcanic ash, desert dust and pollen". *Journal of Quantitative Spectroscopy and Radiative Transfer* 271, p. 107761. ISSN: 0022-4073. DOI: https://doi.org/10.1016/j.jqsrt.2021.107761 (cit. on p. 34).

Goudie, A. S. (2009). "Dust storms: Recent developments". *J. Environ. Manage.* 90.1, pp. 89–94. ISSN: 0301-4797. DOI: https://doi.org/10.1016/j.jenvman.2008.07.007 (cit. on pp. 9, 10).

Griffin, D. W. and C. A. Kellogg (2004). "Dust Storms and Their Impact on Ocean and Human Health: Dust in Earth's Atmosphere". *EcoHealth* 1.3, pp. 284–295. ISSN: 1612-9210. DOI: 10.1007/s10393-004-0120-8 (cit. on p. 10).

Gwaze, P., G. Helas, H. J. Annegarn, J. Huth, and S. J. Piketh (2007). "Physical, chemical and optical properties of aerosol particles collected over Cape Town during winter haze episodes". en. *S. Afr. J. Sci.* 103, pp. 35–43. ISSN: 0038-2353 (cit. on p. 36).

Haarig, M., A. Ansmann, H. Baars, C. Jimenez, I. Veselovskii, R. Engelmann, and D. Althausen (2018). "Depolarization and lidar ratios at 355, 532, and 1064 nm and microphysical properties of aged tropospheric and stratospheric Canadian wildfire smoke". *Atmos. Chem. Phys.* 2018.16, pp. 11847–11861. DOI: 10.5194/acp-18-11847-2018 (cit. on p. 17).

Haarig, M., A. Ansmann, J. Gasteiger, K. Kandler, D. Althausen, H. Baars, M. Radenz, and D. A. Farrell (2017). "Dry versus wet marine particle optical properties: RH dependence of depolarization ratio, backscatter, and extinction from multiwavelength lidar measurements during SALTRACE". *Atmos. Chem. Phys.* 17.23, pp. 14199–14217. DOI: 10.5194/acp-17-14199-2017 (cit. on pp. 7, 36).

Haarig, M., R. Engelmann, A. Ansmann, I. Veselovskii, D. N. Whiteman, and D. Althausen (2016). "1064 nm rotational Raman lidar for particle extinction and lidar-ratio profiling: cirrus case study". *Atmos. Meas. Tech.* 9.9, pp. 4269–4278. DOI: 10.5194/amt-9-4269-2016 (cit. on p. 17).

He, C., K.-N. Liou, Y. Takano, R. Zhang, M. Levy Zamora, P. Yang, Q. Li, and L. R. Leung (2015). "Variation of the radiative properties during black carbon aging: theoretical and experimental intercomparison". *Atmos. Chem. Phys.* 15.20, pp. 11967–11980. DOI: 10.5194/acp-15-11967-2015 (cit. on p. 33).

Hergert, W. and T. Wriedt, eds. (2012). *The Mie Theory - Basics and Applications*. Springer, Berlin, Heidelberg. ISBN: 978-3-642-28738-1. DOI: 10.1007/978-3-642-28738-1 (cit. on p. 26).

Holton, J. R. (2004). *An Introduction to Dynamic Meteorology*. Fourth Edition. Boston: Elsevier Academic Press. ISBN: 0-12-354015-1 (cit. on pp. 5–7).

Hoose, C., J. E. Kristjánsson, J.-P. Chen, and A. Hazra (2010). "A Classical-Theory-Based Parameterization of Heterogeneous Ice Nucleation by Mineral Dust, Soot, and Biological Particles in a Global Climate Model". *J. Atmos. Sci.* 67.8, pp. 2483–2503. DOI: 10.1175/2010JAS3425.1 (cit. on p. 9).

Hulst, H. C. van de (1981). *Light Scattering by Small Particles*. DOVER PUBN INC. 496 pp. ISBN: 978-0-486-64228-4 (cit. on p. 23).

Ishimoto, H., R. Kudo, and K. Adachi (2019). "A shape model of internally mixed soot particles derived from artificial surface tension". *Atmos. Meas. Tech.* 12.1, pp. 107–118. DOI: 10.5194/amt-12-107-2019 (cit. on p. 33).

Jacobson, M. Z. (2001). "Strong radiative heating due to the mixing state of black carbon in atmospheric aerosols". *Nature* 409.6821, pp. 695–697. ISSN: 1476-4687. DOI: 10.1038/35055518 (cit. on p. 32).

Janicka, L. and I. S. Stachlewska (2019). "Properties of biomass burning aerosol mixtures derived at fine temporal and spatial scales from Raman lidar measurements: Part I optical properties". *Atmos. Chem. Phys. Discuss.* 2019, pp. 1–46. DOI: 10.5194/acp-2019-207 (cit. on p. 25).

Järvinen, E. (2016). "Investigations of Angular Light Scattering by Complex Atmospheric Particles". PhD thesis. Karlsruher Institut für Technologie (KIT) (cit. on p. 34).

Jeong, G. Y. and T. Nousiainen (2014). "TEM analysis of the internal structures and mineralogy of Asian dust particles and the implications for optical modeling". *Atmos. Chem. Phys.* 14.14, pp. 7233–7254. DOI: 10.5194/acp-14-7233-2014 (cit. on pp. 34, 35).

Johnson, C., N. K. Nichols, and B. J. Hoskins (2005). "Very large inverse problems in atmosphere and ocean modelling". *Int. J. Numer. Methods Fluids* 47.8-9, pp. 759–771. DOI: 10.1002/fld.869 (cit. on p. 31).

Kahnert, M. (2015). "Modelling radiometric properties of inhomogeneous mineral dust particles: Applicability and limitations of effective medium theories". *J. Quant. Spectrosc. Radiat. Transfer* 152, pp. 16–27. DOI: 10.1016/j.jqsrt.2014.10.025 (cit. on p. 35).

Kahnert, M. and E. Andersson (2017). "How much information do extinction and backscattering measurements contain about the chemical composition of atmo-

spheric aerosol?" *Atmos. Chem. Phys.* 17.5, pp. 3423–3444. DOI: 10.5194/acp-17-3423-2017 (cit. on pp. 37, 38).

Kahnert, M. (2016). "Numerical solutions of the macroscopic Maxwell equations for scattering by non-spherical particles: A tutorial review". *J. Quant. Spectrosc. Radiat. Transfer* 178.Supplement C. Electromagnetic and light scattering by nonspherical particles XV: Celebrating 150 years of Maxwell's electromagnetics, pp. 22–37. DOI: 10.1016/j.jqsrt.2015.10.029 (cit. on p. 26).

Kahnert, M. (2017). "Optical properties of black carbon aerosols encapsulated in a shell of sulfate: comparison of the closed cell model with a coated aggregate model". *Opt. Express* 25.20, pp. 24579–24593. DOI: 10.1364/OE.25.024579 (cit. on pp. 33, 39).

Kahnert, M. and F. Kanngießer (2020). "Modelling optical properties of atmospheric black carbon aerosols". *J. Quant. Spectrosc. Radiat. Transfer* 244, p. 106849. ISSN: 0022-4073. DOI: https://doi.org/10.1016/j.jqsrt.2020.106849 (cit. on p. 40).

Kahnert, M., T. Nousiainen, and H. Lindqvist (2013). "Models for integrated and differential scattering optical properties of encapsulated light absorbing carbon aggregates". *Opt. Express* 21.7, pp. 7974–7993. DOI: 10.1364/OE.21.007974 (cit. on pp. 29, 32).

Kahnert, M., T. Nousiainen, and H. Lindqvist (2014). "Review: Model particles in atmospheric optics". *J. Quant. Spectrosc. Radiat. Transfer* 146.Supplement C. Electromagnetic and Light Scattering by Nonspherical Particles XIV, pp. 41–58. DOI: 10.1016/j.jqsrt.2014.02.014 (cit. on p. 29).

Kahnert, M., T. Nousiainen, M. A. Thomas, and J. Tyynelä (2012). "Light scattering by particles with small-scale surface roughness: Comparison of four classes of model geometries". *J. Quant. Spectrosc. Radiat. Transfer* 113.18. Electromagnetic and Light Scattering by non-spherical particles XIII, pp. 2356–2367. DOI: 10.1016/j.jqsrt.2012.03.017 (cit. on p. 32).

Kalnay, E. (2003). *Atmospheric modeling, data assimilation, and predictability*. Cambridge New York: Cambridge University Press. ISBN: 9780511077845 (cit. on p. 37).

Kandler, K., L. Schütz, C. Deutscher, M. Ebert, H. Hofmann, S. Jäckel, R. Jaenicke, P. Knippertz, K. Lieke, A. Massling, A. Petzold, A. Schladitz, B. Weinzierl, A. Wiedensohler, S. Zorn, and S. Weinbruch1 (2009). "Size distribution, mass concentration, chemical and mineralogical composition and derived optical parameters of the boundary layer aerosol at Tinfou, Morocco, during SAMUM 2006". *Tellus B: Chemical and Physical Meteorology* 61.1, pp. 32–50. DOI: 10.1111/j.1600-0889.2008.00385.x (cit. on p. 34).

Kemppinen, O., T. Nousiainen, and G. Y. Jeong (2015). "Effects of dust particle internal structure on light scattering". *Atmos. Chem. Phys.* 15.20, pp. 12011–12027. DOI: 10.5194/acp-15-12011-2015 (cit. on pp. 34, 35).

King, M. D. and O. Dubovik (2013). "Aerosol Remote Sensing". In: Springer-Verlag GmbH. Chap. Determination of aerosol optical properties from inverse methods, pp. 101–136. ISBN: 978-3-642-17725-5 (cit. on pp. 12, 16).

King, S. M., A. C. Butcher, T. Rosenoern, E. Coz, K. I. Lieke, G. de Leeuw, E. D. Nilsson, and M. Bilde (2012). "Investigating Primary Marine Aerosol Properties: CCN Activity of Sea Salt and Mixed Inorganic-Organic Particles". *Environ. Sci. Technol.* 46.19, pp. 10405–10412. ISSN: 0013-936X. DOI: 10.1021/es300574u (cit. on p. 9).

Klingebiel, M., V. P. Ghate, A. K. Naumann, F. Ditas, M. L. Pöhlker, C. Pöhlker, K. Kandler, H. Konow, and B. Stevens (2019). "Remote Sensing of Sea Salt Aerosol below Trade Wind Clouds". *J. Atmos. Sci.* 76.5, pp. 1189–1202. DOI: 10.1175/JAS-D-18-0139.1 (cit. on p. 13).

Kobziar, L. N. and G. R. Thompson (2020). "Wildfire smoke, a potential infectious agent". *Science* 370.6523, pp. 1408–1410. ISSN: 0036-8075. DOI: 10.1126/science.abe8116 (cit. on p. 10).

Krishnamurti, T. N., L. Stefanova, and vasubandhu Misra (2013). *Tropical Meteorology: An Introduction*. Springer Atmospheric Sciences. New York, NY: Springer New York. ISBN: 9781461474098. DOI: 10.1007/978-1-4614-7409-8 (cit. on p. 7).

Kumar, R., M. C. Barth, G. G. Pfister, M. Naja, and G. P. Brasseur (2014). "WRF-Chem simulations of a typical pre-monsoon dust storm in northern India: influences on aerosol optical properties and radiation budget". *Atmos. Chem. Phys.* 14.5, pp. 2431–2446. DOI: 10.5194/acp-14-2431-2014 (cit. on p. 9).

Lenoble, J., L. A. Remer, and D. Tanré (2013). "Aerosol Remote Sensing". In: Springer-Verlag GmbH. Chap. Introduction, pp. 1–11. ISBN: 978-3-642-17725-5 (cit. on p. 11).

Li, Q., D. Zheng, Y. Wang, R. Li, H. Wu, S. Xu, Y. Kang, Y. Cao, X. Chen, Y. Zhu, S. Xu, Z.-J. Chen, P. Liu, and J. Qiao (2021). "Association between exposure to airborne particulate matter less than 2.5 μm and human fecundity in China". *Environ. Int.* 146, p. 106231. ISSN: 0160-4120. DOI: https://doi.org/10.1016/j.envint.2020.106231 (cit. on p. 10).

Lin, W., L. Bi, and O. Dubovik (2018). "Assessing Superspheroids in Modeling the Scattering Matrices of Dust Aerosols". *Journal of Geophysical Research: Atmospheres* 123.24, pp. 13, 917–13, 943. DOI: https://doi.org/10.1029/2018JD029464 (cit. on p. 34).

Liou, K., Y. Takano, and P. Yang (2011). "Light absorption and scattering by aggregates: Application to black carbon and snow grains". *J. Quant. Spectrosc. Radiat. Transfer* 112.10, pp. 1581–1594. DOI: 10.1016/j.jqsrt.2011.03.007 (cit. on p. 33).

Liu, C., J. Li, Y. Yin, B. Zhu, and Q. Feng (2017). "Optical properties of black carbon aggregates with non-absorptive coating". *J. Quant. Spectrosc. Radiat. Transfer* 187, pp. 443–452. ISSN: 0022-4073. DOI: https://doi.org/10.1016/j.jqsrt.2016.10.023 (cit. on p. 33).

Liu, C., R. L. Panetta, P. Yang, A. Macke, and A. J. Baran (2013). "Modeling the scattering properties of mineral aerosols using concave fractal polyhedra". *Appl. Opt.* 52.4, pp. 640–652. DOI: 10.1364/AO.52.000640 (cit. on p. 35).

Liu, C., Y. Yin, F. Hu, H. Jin, and C. M. Sorensen (2015a). "The Effects of Monomer Size Distribution on the Radiative Properties of Black Carbon Aggregates".

Aerosol Sci. Technol. 49.10, pp. 928–940. DOI: 10.1080/02786826.2015.1085953 (cit. on p. 31).

Liu, F., J. Yon, and A. Bescond (2016). "On the radiative properties of soot aggregates – Part 2: Effects of coating". *J. Quant. Spectrosc. Radiat. Transfer* 172.Supplement C, pp. 134–145. DOI: 10.1016/j.jqsrt.2015.08.005 (cit. on p. 32).

Liu, J. C., G. Pereira, S. A. Uhl, M. A. Bravo, and M. L. Bell (2015b). "A systematic review of the physical health impacts from non-occupational exposure to wildfire smoke". *Environ. Res.* 136, pp. 120–132. ISSN: 0013-9351. DOI: https://doi.org/10.1016/j.envres.2014.10.015 (cit. on p. 10).

Liu, J., P. Yang, and K. Muinonen (2015c). "Dust-aerosol optical modeling with Gaussian spheres: Combined invariant-imbedding T-matrix and geometric-optics approach". *J. Quant. Spectrosc. Radiat. Transfer* 161, pp. 136–144. ISSN: 0022-4073. DOI: https://doi.org/10.1016/j.jqsrt.2015.04.003 (cit. on p. 35).

Liu, L. and M. I. Mishchenko (2018). "Scattering and Radiative Properties of Morphologically Complex Carbonaceous Aerosols: A Systematic Modeling Study". *Remote Sens.* 10.10. ISSN: 2072-4292. DOI: 10.3390/rs10101634 (cit. on p. 33).

Liu, L., M. I. Mishchenko, and W. P. Arnott (2008). "A study of radiative properties of fractal soot aggregates using the superposition T-matrix method". *J. Quant. Spectrosc. Radiat. Transfer* 109.15. DOI: 10.1016/j.jqsrt.2008.05.001 (cit. on p. 31).

Luo, J., Y. Zhang, and Q. Zhang (2018). "A model study of aggregates composed of spherical soot monomers with an acentric carbon shell". *J. Quant. Spectrosc. Radiat. Transfer* 205, pp. 184–195. ISSN: 0022-4073. DOI: 10.1016/j.jqsrt.2017.10.024 (cit. on p. 33).

Mackowski, D. W. and M. I. Mishchenko (1996). "Calculation of the T matrix and the scattering matrix for ensembles of spheres". *J. Opt. Soc. Am. A* 13, pp. 2266–2278 (cit. on p. 26).

Mackowski, D. W. (2006). "A simplified model to predict the effects of aggregation on the absorption properties of soot particles". *J. Quant. Spectrosc. Radiat. Transfer* 100.1. VIII Conference on Electromagnetic and Light Scattering by Nonspherical Particles, pp. 237–249. DOI: 10.1016/j.jqsrt.2005.11.041 (cit. on p. 30).

Mahowald, N. M., R. Scanza, J. Brahney, C. L. Goodale, P. G. Hess, J. K. Moore, and J. Neff (2017). "Aerosol Deposition Impacts on Land and Ocean Carbon Cycles". *Current Climate Change Reports* 3.1, pp. 16–31. ISSN: 2198-6061. DOI: 10.1007/s40641-017-0056-z (cit. on p. 10).

Mayer, B. and A. Kylling (2005). "Technical note: The libRadtran software package for radiative transfer calculations - description and examples of use". *Atmos. Chem. Phys.* 5.7, pp. 1855–1877. DOI: 10.5194/acp-5-1855-2005 (cit. on p. 20).

McCormick, M. P. and K. R. Leavor (2013). "Aerosol Remote Sensing". In: Springer-Verlag GmbH. Chap. Active lidar remote sensing, pp. 283–313. ISBN: 978-3-642-17725-5 (cit. on p. 6).

McInnes, L. M., D. S. Covert, P. K. Quinn, and M. S. Germani (1994). "Measurements of chloride depletion and sulfur enrichment in individual sea-salt particles collected from the remote marine boundary layer". *Journal of Geophysical Re-*

search: Atmospheres 99.D4, pp. 8257–8268. DOI: 10.1029/93JD03453 (cit. on p. 36).

Meira, G., C. Andrade, C. Alonso, I. Padaratz, and J. Borba (2008). "Modelling sea-salt transport and deposition in marine atmosphere zone – A tool for corrosion studies". *Corros. Sci.* 50.9, pp. 2724–2731. ISSN: 0010-938X. DOI: https://doi.org/10.1016/j.corsci.2008.06.028 (cit. on p. 10).

Merikallio, S., T. Nousiainen, M. Kahnert, and A.-M. Harri (2013). "Light scattering by the Martian dust analog, palagonite, modeled with ellipsoids". *Opt. Express* 21.15, pp. 17972–17985. DOI: 10.1364/OE.21.017972 (cit. on p. 34).

Mie, G. (1908). "Beiträge zur Optik trüber Medien, speziell kolloidaler Metalllösungen". *Ann. Phys.* 330.3, pp. 377–445. DOI: 10.1002/andp.19083300302 (cit. on p. 26).

Miffre, A. (2015). "LIGHT BACKSCATTERING BY ATMOSPHERIC PARTICLES: LABORATORY AND FIELD EXPERIMENTS". habilitation thesis. CLAUDE BERNARD LYON 1 UNIVERSITY (cit. on p. 17).

Mishchenko, M. I. and J. W. Hovenier (1995). "Depolarization of light backscattered by randomly oriented nonspherical particles". *Opt. Lett.* 20.12, pp. 1356–1358. DOI: 10.1364/OL.20.001356 (cit. on p. 25).

Mishchenko, M. I., L. D. Travis, and A. A. Lacis (2006). *Multiple Scattering of Light by Particles: Radiative Transfer and Coherent Backscattering*. Cambridge: Cambridge University Press. 510 pp. ISBN: 978-0-521-83490-2 (cit. on p. 21).

Mishchenko, M. I., J. M. Dlugach, and L. Liu (2016). "Linear depolarization of lidar returns by aged smoke particles". *Appl. Opt.* 55.35. DOI: 10.1364/AO.55.009968 (cit. on p. 33).

Mishchenko, M. I., L. D. Travis, R. A. Kahn, and R. A. West (1997). "Modeling phase functions for dustlike tropospheric aerosols using a shape mixture of randomly oriented polydisperse spheroids". *J. Geophys. Res.* 102.D14, pp. 16831–16847. DOI: 10.1029/96JD02110 (cit. on p. 34).

Mishchenko, M. I., L. D. Travis, and A. A. Lacis (2002). *Scattering, Absorption, and Emission of Light by Small Particles*. CAMBRIDGE UNIVERSITY PRESS. ISBN: 9780521782524 (cit. on pp. 21–24).

Muinonen, K., T. Nousiainen, P. Fast, K. Lumme, and J. Peltoniemi (1996). "Light scattering by Gaussian random particles: Ray optics approximation". *J. Quant. Spectrosc. Radiat. Transfer* 55.5. Light Scattering by Non-Spherical Particles, pp. 577–601. ISSN: 0022-4073. DOI: 10.1016/0022-4073(96)00003-9 (cit. on p. 35).

Müller, D., U. Wandinger, and A. Ansmann (1999). "Microphysical particle parameters from extinction and backscatter lidar data by inversion with regularization: theory". *Appl. Opt.* 38.12, pp. 2346–2357. DOI: 10.1364/AO.38.002346 (cit. on p. 15).

Muñoz, O., F. Moreno, D. Guirado, D. Dabrowska, H. Volten, and J. Hovenier (2012). "The Amsterdam–Granada Light Scattering Database". *J. Quant. Spectrosc. Radiat. Transfer* 113.7, pp. 565–574. ISSN: 0022-4073. DOI: 10.1016/j.jqsrt.2012.01.014 (cit. on p. 34).

Muñoz, O., H. Volten, J. W. Hovenier, T. Nousiainen, K. Muinonen, D. Guirado, F. Moreno, and L. B. F. M. Waters (2007). "Scattering matrix of large Saharan dust particles: Experiments and computations". *Journal of Geophysical Research: Atmospheres* 112.D13. DOI: https://doi.org/10.1029/2006JD008074 (cit. on pp. 34, 35).

Murayama, T. H., H. Okamoto, N. Kaneyasu, H. Kamataki, and K. Miura (1999). "Application of lidar depolarization measurement in the atmospheric boundary layer: Effects of dust and sea-salt particles". *J. Geophys. Res.* 104.D24, pp. 31781–31792. DOI: 10.1029/1999JD900503 (cit. on p. 36).

Murphy, D. M., J. R. Anderson, P. K. Quinn, L. M. McInnes, F. J. Brechtel, S. M. Kreidenweis, A. M. Middlebrook, M. Pósfai, D. S. Thomson, and P. R. Buseck (1998). "Influence of sea-salt on aerosol radiative properties in the Southern Ocean marine boundary layer". *Nature* 392.6671, pp. 62–65. ISSN: 1476-4687. DOI: 10.1038/32138 (cit. on p. 9).

Murray, B. J., O. O'Sullivan, J. D. Atkinson, and M. Webb (2012). "Ice nucleation by particles immersed in supercooled cloud droplets". *Chem. Soc. Rev.* 41, pp. 6519–6554. DOI: 10.1039/C2CS35200A (cit. on p. 9).

Murray, C. J. L. et al. (2020). "Global burden of 87 risk factors in 204 countries and territories, 1990–2019: a systematic analysis for the Global Burden of Disease Study 2019". *The Lancet* 396.10258, pp. 1223–1249. DOI: 10.1016/S0140-6736(20)30752-2 (cit. on p. 3).

Myhre, G., D. Shindell, F.-M. Bréon, W. Collins, J. Fuglestvedt, J. Huang, D. Koch, J.-F. Lamarque, D. Lee, B. Mendoza, T. Nakajima, A. Robock, G. Stephens, T. Takemura, and H. Zhang (2013). "Anthropogenic and Natural Radiative Forcing". In: *Climate Change 2013: The Physical Science Basis. Contribution of Working Group I to the Fifth Assessment Report of the Intergovernmental Panel on Climate Change*. Ed. by T. Stocker, D. Qin, G.-K. Plattner, M. Tignor, S. Allen, J. Boschung, A. Nauels, Y. Xia, V. Bex, and P. Midgley. Cambridge, United Kingdom and New York, NY, USA: Cambridge University Press. Chap. 8, pp. 659–740. ISBN: ISBN 978-1-107-66182-0. DOI: 10.1017/CBO9781107415324.018 (cit. on p. 10).

Naik, V., S. Szopa, B. Adhikary, P. Artaxo, T. Berntsen, W. D. Collins, S. Fuzzi, L. Gallardo, A. K. Scharr, Z. Klimont, H. Liao, N. Unger, and P. Zanis (2021). "Short-Lived Climate Forcers". In: *Climate Change 2021: The Physical Science Basis. Contribution of Working Group I to the Sixth Assessment Report of the Intergovernmental Panel on Climate Change*. Ed. by V. Masson-Delmotte, P. Zhai, A. Pirani, S. L. Connors, C. Péan, S. Berger, N. Caud, Y. Chen, L. Goldfarb, M. I. Gomis, M. Huang, K. Leitzell, E. Lonnoy, J. B. R. Matthews, T. K. Maycock, T. Waterfield, O. Yelekçi, R. Yu, and B. Zhou. Cambridge University Press. Chap. 6 (cit. on pp. 3, 9, 10).

Nousiainen, T., M. Kahnert, and H. Lindqvist (2011). "Can particle shape information be retrieved from light-scattering observations using spheroidal model particles?" *J. Quant. Spectrosc. Radiat. Transfer* 112.13. Polarimetric Detection, Characterization, and Remote Sensing, pp. 2213–2225. ISSN: 0022-4073. DOI: https://doi.org/10.1016/j.jqsrt.2011.05.008 (cit. on p. 34).

Nousiainen, T., M. Kahnert, and B. Veihelmann (2006). "Light scattering modeling of small feldspar aerosol particles using polyhedral prisms and spheroids". *J. Quant. Spectrosc. Radiat. Transfer* 101.3. Light in Planetary Atmospheres and Other Particulate Media, pp. 471–487. ISSN: 0022-4073. DOI: https://doi.org/10.1016/j.jqsrt.2006.02.038 (cit. on pp. 34, 35).

Pei, X. (2018). "A Soot Transformation Study: Interactions Between Soot, Sulfuric Acid and Secondary Organic Aerosol (SOA)". PhD thesis. University of Gothenburg. Faculty of Science. URL: http://hdl.handle.net/2077/54249 (cit. on p. 32).

Petty, G. (2006). *A First Course In Atmospheric Radiation*. 2nd ed. Madison, Wisconsin: Sundog Publishing. ISBN: 978-0-9729033-1-8 (cit. on p. 19).

Pöschl, U. (2005). "Atmospheric Aerosols: Composition, Transformation, Climate and Health Effects". *Angew. Chem. Int. Ed.* 44.46, pp. 7520–7540. DOI: 10.1002/anie.200501122 (cit. on p. 10).

Post, M. J., C. J. Grund, A. M. Weickmann, K. R. Healy, and R. J. Willis (1996). "Comparison of Mount Pinatubo and El Chichon volcanic events: Lidar observations at 10.6 and 0.69 μm". *Journal of Geophysical Research: Atmospheres* 101.D2, pp. 3929–3940. DOI: https://doi.org/10.1029/95JD02926 (cit. on p. 15).

Pravia-Sarabia, E., J. J. Gómez-Navarro, P. Jiménez-Guerrero, and J. P. Montávez (2021). "Influence of sea salt aerosols on the development of Mediterranean tropical-like cyclones". *Atmos. Chem. Phys. Discuss.* 2021, pp. 1–18. DOI: 10.5194/acp-2020-1312 (cit. on p. 10).

Purcell, E. M. and C. R. Pennypacker (1973). "Scattering and absorption of light by nonspherical dielectric grains". *Astrophys. J.* 186, pp. 705–714. DOI: 10.1086/152538 (cit. on p. 26).

Quirantes, A. (2005). "A T-matrix method and computer code for randomly oriented, axially symmetric coated scatterers". *J. Quant. Spectrosc. Radiat. Transfer* 92.3, pp. 373–381. ISSN: 0022-4073. DOI: https://doi.org/10.1016/j.jqsrt.2004.08.004 (cit. on p. 26).

Rodgers, C. D. (2000). *Inverse methods for atmospheric sounding : theory and practice*. Singapore River Edge, N.J: World Scientific. ISBN: 9789812813718 (cit. on p. 37).

Sakai, T., T. Nagai, Y. Zaizen, and Y. Mano (2010). "Backscattering linear depolarization ratio measurements of mineral, sea-salt, and ammonium sulfate particles simulated in a laboratory chamber". *Appl. Opt.* 49.23, pp. 4441–4449. DOI: 10.1364/AO.49.004441 (cit. on p. 36).

Sasano, Y. and E. V. Browell (1989). "Light scattering characteristics of various aerosol types derived from multiple wavelength lidar observations". *Appl. Opt.* 28.9, pp. 1670–1679. DOI: 10.1364/AO.28.001670 (cit. on p. 15).

Sassen, K. (2005). "Polarisation in Lidar". In: *Lidar: Range-Resolved Optical Remote Sensing of the Atmosphere*. Ed. by C. Weitkamp. New York, NY: Springer New York, pp. 19–42. ISBN: 978-0-387-25101-1. DOI: 10.1007/0-387-25101-4_1 (cit. on p. 14).

Schmidt, W. C. (2016). "Pollen Overload: Seasonal Allergies in a Changing Climate". *Environ. Health Perspect.* 124.4, A70–A75. DOI: 10.1289/ehp.124-A70 (cit. on p. 10).

Schnaiter, M., S. Büttner, O. Möhler, J. Skrotzki, M. Vragel, and R. Wagner (2012). "Influence of particle size and shape on the backscattering linear depolarisation ratio of small ice crystals - cloud chamber measurements in the context of contrail and cirrus microphysics". *Atmos. Chem. Phys.* 12.21, pp. 10465–10484. DOI: 10.5194/acp-12-10465-2012 (cit. on p. 25).

Schnitzler, E. G., A. Dutt, A. M. Charbonneau, J. S. Olfert, and W. Jäger (2014). "Soot Aggregate Restructuring Due to Coatings of Secondary Organic Aerosol Derived from Aromatic Precursors". *Environ. Sci. Technol.* 48.24. PMID: 25390075, pp. 14309–14316. DOI: 10.1021/es503699b (cit. on p. 32).

Seinfeld, J. H. and S. N. Pandis (2016). *Atmospheric Chemistry and Physics : From Air Pollution to Climate Change*. New York, United States: John Wiley & Sons, Incorporated. ISBN: 9781119221166 (cit. on pp. 5, 6, 10).

Shaddick, G., M. L. Thomas, P. Mudu, G. Ruggeri, and S. Gumy (2020). "Half the world's population are exposed to increasing air pollution". *npj Climate and Atmospheric Science* 3.1, p. 23. ISSN: 2397-3722. DOI: 10.1038/s41612-020-0124-2 (cit. on p. 3).

Skorupski, K. and J. Mroczka (2014). "Effect of the necking phenomenon on the optical properties of soot particles". *J. Quant. Spectrosc. Radiat. Transfer* 141.Supplement C, pp. 40–48. ISSN: 0022-4073. DOI: 10.1016/j.jqsrt.2014.03.001 (cit. on p. 31).

Sorensen, C. M. (2001). "Light Scattering by Fractal Aggregates: A Review". *Aerosol Sci. Technol.* 35, pp. 648–687. DOI: 10.1080/02786820117868 (cit. on pp. 29, 30).

Steiner, A. L., S. D. Brooks, C. Deng, D. C. O. Thornton, M. W. Pendleton, and V. Bryant (2015). "Pollen as atmospheric cloud condensation nuclei". *Geophysical Research Letters* 42.9, pp. 3596–3602. DOI: https://doi.org/10.1002/2015GL064060 (cit. on p. 9).

Stull, R. B. (1988). "Mean Boundary Layer Characteristics". In: *An Introduction to Boundary Layer Meteorology*. Ed. by R. B. Stull. Dordrecht: Springer Netherlands, pp. 1–27. ISBN: 978-94-009-3027-8. DOI: 10.1007/978-94-009-3027-8_1 (cit. on pp. 5–7).

Takano, Y. and K. Jayaweera (1985). "Scattering phase matrix for hexagonal ice crystals computed from ray optics". *Appl. Opt.* 24.19, pp. 3254–3263. DOI: 10.1364/AO.24.003254 (cit. on p. 25).

Teng, S., C. Liu, M. Schnaiter, R. K. Chakrabarty, and F. Liu (2019). "Accounting for the effects of nonideal minor structures on the optical properties of black carbon aerosols". *Atmos. Chem. Phys.* 19.5, pp. 2917–2931. DOI: 10.5194/acp-19-2917-2019 (cit. on p. 31).

Tesche, M., A. Ansmann, D. Müller, D. Althausen, R. Engelmann, V. Freudenthaler, and S. Groß (2009). "Vertically resolved separation of dust and smoke over Cape Verde using multiwavelength Raman and polarization lidars during Saharan Mineral Dust Experiment 2008". *J. Geophys. Res. Atmos.* 114.D13. DOI: https://doi.org/10.1029/2009JD011862 (cit. on p. 17).

Tesche, M., A. Kolgotin, M. Haarig, S. P. Burton, R. A. Ferrare, C. A. Hostetler, and D. Müller (2019). "3+2+X: what is the most useful depolarization input for retrieving

microphysical properties of non-spherical particles from lidar measurements using the spheroid model of Dubovik et al. (2006)?" *Atmos. Meas. Tech.* 12.8, pp. 4421–4437. DOI: 10.5194/amt-12-4421-2019 (cit. on p. 17).

Torge, A., A. Macke, B. Heinold, and J. Wauer (2011). "Solar radiative transfer simulations in Saharan dust plumes: particle shapes and 3-D effect". *Tellus B* 63.4, pp. 770–780. DOI: 10.1111/j.1600-0889.2011.00560.x (cit. on p. 35).

U.S. Commitee on Extension of the Standard Atmosphere (1976). *U.S. Standard Atmosphere*. Tech. rep. U.S. Government Printing Office. URL: https://ntrs.nasa.gov/archive/nasa/casi.ntrs.nasa.gov/19770009539.pdf (cit. on p. 6).

Veihelmann, B., T. Nousiainen, M. Kahnert, and W. van der Zande (2006). "Light scattering by small feldspar particles simulated using the Gaussian random sphere geometry". *J. Quant. Spectrosc. Radiat. Transfer* 100.1. VIII Conference on Electromagnetic and Light Scattering by Nonspherical Particles, pp. 393–405. ISSN: 0022-4073. DOI: https://doi.org/10.1016/j.jqsrt.2005.11.053 (cit. on p. 35).

Veselovskii, I., P. Goloub, T. Podvin, D. Tanre, A. da Silva, P. Colarco, P. Castellanos, M. Korenskiy, Q. Hu, D. N. Whiteman, D. Pérez-Ramírez, P. Augustin, M. Fourmentin, and A. Kolgotin (2018). "Characterization of smoke and dust episode over West Africa: comparison of MERRA-2 modeling with multiwavelength Mie–Raman lidar observations". *Atmos. Meas. Tech.* 11.2, pp. 949–969. DOI: 10.5194/amt-11-949-2018 (cit. on p. 17).

Wandinger, U. (2005). "Introduction to Lidar". In: *Lidar: Range-Resolved Optical Remote Sensing of the Atmosphere*. Ed. by C. Weitkamp. New York, NY: Springer New York, pp. 1–18. ISBN: 978-0-387-25101-1. DOI: 10.1007/0-387-25101-4_1 (cit. on pp. 13, 17).

Waterman, P. C. (1965). "Matrix formulation of electromagnetic scattering". *Proc. IEEE* 53.8, pp. 805–812. ISSN: 0018-9219. DOI: 10.1109/PROC.1965.4058 (cit. on p. 26).

Wells, N. C. (2011). *The Atmosphere and Ocean: A Physical Introduction*. 3rd Edition. John Wiley & Sons, Inc. (cit. on pp. 5, 6).

Wiegner, M., J. Gasteiger, K. Kandler, B. Weinzierl, K. Rasp, M. Esselborn, V. Freudenthaler, B. Heese, C. Toledano, M. Tesche, and D. Althausen (2009). "Numerical simulations of optical properties of Saharan dust aerosols with emphasis on lidar applications". *Tellus B* 61.1, pp. 180–194. DOI: 10.1111/j.1600-0889.2008.00381.x (cit. on p. 34).

Wise, M. E., G. Biskos, S. T. Martin, L. M. Russell, and P. R. Buseck (2005). "Phase Transitions of Single Salt Particles Studied Using a Transmission Electron Microscope with an Environmental Cell". *Aerosol Sci. Technol.* 39.9, pp. 849–856. DOI: 10.1080/02786820500295263 (cit. on p. 36).

Wood, R. (2012). "Stratocumulus Clouds". *Mon. Weather Rev.* 140.8, pp. 2373–2423. DOI: 10.1175/MWR-D-11-00121.1 (cit. on p. 7).

World Health Organization (2016). *Ambient air pollution: A global assessment of exposure and burden of disease*. Tech. rep. World Health Organization. URL: https:

//www.who.int/phe/publications/air-pollution-global-assessment/en/ (cit. on p. 3).

World Meteorological Organization (1992). *International meteorological vocabulary*. Geneva, Switzerland: Secretariat of the World Meteorological Organization. ISBN: 978-92-63-02182-3 (cit. on p. 6).

Worringen, A., M. Ebert, T. Trautmann, S. Weinbruch, and G. Helas (2008). "Optical properties of internally mixed ammonium sulfate and soot particles–a study of individual aerosol particles and ambient aerosol populations". *Appl. Opt.* 47.21, pp. 3835–3845. DOI: 10.1364/AO.47.003835 (cit. on pp. 31, 32).

Wriedt, T. (2002). "Using the T-Matrix Method for Light Scattering Computations by Non-axisymmetric Particles: Superellipsoids and Realistically Shaped Particles". *Part. Part. Sys. Charact.* 19.4, pp. 256–268. DOI: 10.1002/1521-4117(200208)19:4<256::AID-PPSC256>3.0.CO;2-8 (cit. on p. 36).

Wu, Y., T. Cheng, X. Gu, L. Zheng, H. Chen, and H. Xu (2014). "The single scattering properties of soot aggregates with concentric core–shell spherical monomers". *J. Quant. Spectrosc. Radiat. Transfer* 135.Supplement C, pp. 9–19. ISSN: 0022-4073. DOI: 10.1016/j.jqsrt.2013.11.009 (cit. on p. 33).

Wu, Y., T. Cheng, L. Zheng, and H. Chen (2016). "Models for the optical simulations of fractal aggregated soot particles thinly coated with non-absorbing aerosols". *J. Quant. Spectrosc. Radiat. Transfer* 182.Supplement C, pp. 1–11. DOI: 10.1016/j.jqsrt.2016.05.011 (cit. on p. 33).

Wu, Y., T. Cheng, L. Zheng, and H. Chen (2017). "Sensitivity of mixing states on optical properties of fresh secondary organic carbon aerosols". *J. Quant. Spectrosc. Radiat. Transfer* 195.Supplement C, pp. 147–155. DOI: 10.1016/j.jqsrt.2017.01.013 (cit. on p. 32).

Wu, Y., T. Cheng, L. Zheng, H. Chen, and H. Xu (2015). "Single scattering properties of semi-embedded soot morphologies with intersecting and non-intersecting surfaces of absorbing spheres and non-absorbing host". *J. Quant. Spectrosc. Radiat. Transfer* 157.Supplement C, pp. 1–13. ISSN: 0022-4073. DOI: 10.1016/j.jqsrt.2015.02.006 (cit. on pp. 33, 41).

Xiong, C. and S. K. Friedlander (2001). "Morphological properties of atmospheric aerosol aggregates". *Proc. Natl. Acad. Sci. U.S.A.* 98.21, pp. 11851–11856. ISSN: 0027-8424. DOI: 10.1073/pnas.211376098 (cit. on pp. 29, 30).

Yon, J., A. Bescond, and F. Liu (2015). "On the radiative properties of soot aggregates part 1: Necking and overlapping". *J. Quant. Spectrosc. Radiat. Transfer* 162.Supplement C. DOI: 10.1016/j.jqsrt.2015.03.027 (cit. on p. 31).

Yu, H., M. Chin, T. Yuan, H. Bian, L. A. Remer, J. M. Prospero, A. Omar, D. Winker, Y. Yang, Y. Zhang, Z. Zhang, and C. Zhao (2015). "The fertilizing role of African dust in the Amazon rainforest: A first multiyear assessment based on data from Cloud-Aerosol Lidar and Infrared Pathfinder Satellite Observations". *Geophys. Res. Lett.* 42.6, pp. 1984–1991. DOI: https://doi.org/10.1002/2015GL063040 (cit. on p. 10).

Yu, P., O. B. Toon, C. G. Bardeen, Y. Zhu, K. H. Rosenlof, R. W. Portmann, T. D. Thornberry, R.-S. Gao, S. M. Davis, E. T. Wolf, J. de Gouw, D. A. Peterson, M. D. Fromm, and A. Robock (2019). "Black carbon lofts wildfire smoke high

into the stratosphere to form a persistent plume". *Science* 365.6453, pp. 587–590. ISSN: 0036-8075. DOI: 10.1126/science.aax1748 (cit. on p. 8).

Yurkin, M. A. and A. G. Hoekstra (2007). "The discrete dipole approximation: An overview and recent developments". *J. Quant. Spectrosc. Radiat. Transfer* 106.1. IX Conference on Electromagnetic and Light Scattering by Non-Spherical Particles, pp. 558–589. DOI: 10.1016/j.jqsrt.2007.01.034 (cit. on p. 26).

Yurkin, M. A. and A. G. Hoekstra (2011). "The discrete-dipole-approximation code ADDA: Capabilities and known limitations". *J. Quant. Spectrosc. Radiat. Transfer* 112.13, pp. 2234–2247. DOI: 10.1016/j.jqsrt.2011.01.031 (cit. on p. 26).

Zdunkowski, W., T. Trautmann, and A. Bott (2007). *Radiation in the atmosphere: a course in theoretical meteorology*. Cambridge University Press. ISBN: 978-1-108-46272-3 (cit. on pp. 19, 21, 23).

Zeng, J., G. Zhang, S. Long, K. Liu, L. Cao, L. Bao, and Y. Li (2013). "Sea salt deliquescence and crystallization in atmosphere: an in situ investigation using x-ray phase contrast imaging". *Surf. Interface Anal.* 45.5, pp. 930–936. DOI: 10.1002/sia.5184 (cit. on p. 36).

Zerefos, C. S., V. T. Gerogiannis, D. Balis, S. C. Zerefos, and A. Kazantzidis (2007). "Atmospheric effects of volcanic eruptions as seen by famous artists and depicted in their paintings". *Atmos. Chem. Phys.* 7.15, pp. 4027–4042. DOI: 10.5194/acp-7-4027-2007 (cit. on p. 3).

Zhang, R., A. F. Khalizov, J. Pagels, D. Zhang, H. Xue, and P. H. McMurry (2008). "Variability in morphology, hygroscopicity, and optical properties of soot aerosols during atmospheric processing". *Proc. Natl. Acad. Sci. U.S.A.* 105.30, pp. 10291–10296. DOI: 10.1073/pnas.0804860105 (cit. on pp. 31, 32).